

Further evidence for a variable fine-structure constant from Keck/HIRES QSO absorption spectra

M. T. Murphy,^{1,2?} J. K. Webb^{2?}, V. V. Flambaum²

¹*Institute of Astronomy, University of Cambridge, Madingley Road, Cambridge, CB3 0HA, UK*

²*School of Physics, University of New South Wales, UNSW Sydney N.S.W. 2052, Australia*

Accepted —. Received —; in original form —

ABSTRACT

We have previously presented evidence for a varying fine-structure constant, α , in two independent samples of Keck/HIRES QSO absorption spectra. Here we present a detailed many-multiplet analysis of a third Keck/HIRES sample containing 78 absorption systems. We also re-analyse the previous samples, providing a total of 128 absorption systems over the redshift range $0.2 < z_{\text{abs}} < 3.7$. The results, with raw statistical errors, indicate a smaller weighted mean α in the absorption clouds: $\alpha = (0.574 \pm 0.02) \times 10^{-5}$. All three samples separately yield consistent and significant values of $\alpha = 0$. The analyses of low- z (i.e. $z_{\text{abs}} < 1.8$) and high- z systems rely on different ions and transitions with very different dependencies on α , yet they also give consistent results. We identify an additional source of random error in 22 high- z systems characterized by transitions with a large dynamic range in apparent optical depth. Increasing the statistical errors on α for these systems gives our fiducial result, a weighted mean $\alpha = (0.543 \pm 0.116) \times 10^{-5}$, representing 4.7 evidence for a varying α . Assuming that $\alpha = 0$ at $z_{\text{abs}} = 0$, the data marginally prefer a linear increase in α with time rather than a constant offset from the laboratory value: $\dot{\alpha} = (6.40 \pm 1.35) \times 10^{-16} \text{ yr}^{-1}$. The two-point correlation function for α is consistent with zero over 0.2–13 Gpc comoving scales and the angular distribution of α shows no significant dipolar anisotropy. We therefore have no evidence for spatial variations in α .

We extend our previous searches for possible systematic errors, giving detailed analyses of potential kinematic effects, line blending, wavelength miscalibration, spectrograph temperature variations, atmospheric dispersion and isotopic/hyperfine structure effects. The latter two are potentially the most significant. However, overall, known systematic errors do not explain the results. Future many-multiplet analyses of independent QSO spectra from different telescopes and spectrographs will provide a now crucial check on our Keck/HIRES results.

Key words: atomic data – line: profiles – methods: laboratory – techniques: spectroscopic – quasars: absorption lines – ultraviolet: general

1 INTRODUCTION

High resolution spectroscopy of QSO absorption systems provides a precise probe of possible variations in several fundamental constants over cosmological distances and timescales. Dzuba, Flambaum & Webb (1999a,b) and Webb et al. (1999) introduced and applied the new and highly sensitive many-multiplet (MM) method for constraining space-time variations of the fine-structure constant,

$\alpha = h c / (m_e e^2)$. Using a MM analysis of 49 absorption systems from two independent samples of Keck/HIRES spectra, we recently reported statistical evidence for a variable α (Murphy et al. 2001a, hereafter M01a; Webb et al. 2001): $\alpha = (0.72 \pm 0.18) \times 10^{-5}$, where α is defined as

$$\alpha = \left(\frac{z}{z_0} - 1 \right) / \alpha_0 = 0 \quad (1)$$

for z and z_0 the values of α in the absorption system(s) and in the laboratory respectively¹. The absorption redshifts covered the range $0.5 < z_{\text{abs}} < 3.5$.

Here we significantly extend this work, presenting new measurements of α in a third independent Keck/HIRES sample of 78 absorption systems covering the range $0.2 < z_{\text{abs}} < 3.7$. The present paper provides a detailed description of our methods, results and analysis of potential systematic effects. A companion paper, Webb et al. (in preparation), presents a summary of the main results.

In the remainder of this section we outline the many multiplet technique of obtaining constraints on α from QSO spectra. We

? E-mail: mim@ast.cam.ac.uk (MTM); jkw@phys.unsw.edu.au (JKW)

¹ $\alpha_0^{-1} = 137.03599958(52)$ (Mohr & Taylor 2000).

describe the different QSO and atomic datasets in Section 2 and our analysis methods in Section 3. The new results, together with those from a re-analysis of the previous datasets, are presented in Section 4. We consider both temporal and spatial variations in λ . Section 5 extends our search for systematic errors, concentrating on those difficult to quantify in Murphy et al. (2001b, hereafter M01b). We summarize the present work in Section 6 and compare our new values of λ with other constraints on λ -variation.

1.1 QSO absorption line constraints on λ

1.1.1 The alkali-doublet (AD) method

The relative wavelength separation between the two transitions of an alkali doublet (AD) is proportional to λ^{-2} (e.g. Bethe & Salpeter 1977). Savedoff (1956) first analysed AD separations seen in Seyfert galaxy emission spectra to obtain constraints on λ -variation. Absorption lines from intervening clouds along the line of sight to QSOs are substantially narrower than intrinsic emission lines and therefore provide a more precise probe. Bahcall, Sargent & Schmidt (1967) first used AD absorption lines which seemed to be intrinsic to the QSO. Narrower still are absorption lines arising from gas clouds at significantly lower redshift than the background QSO. Wolfe, Brown & Roberts (1976) first analysed Mg II doublets from a damped Lyman- α system at $z_{\text{abs}} = 0.524$. Since then, several authors (e.g. Cowie & Songaila 1995; Varshalovich et al. 1996, 2000) have applied the AD method to doublets of several different species (e.g. C IV, Si II, Si IV, Mg II and Al III).

In Murphy et al. (2001c) we obtained the strongest current AD constraint on λ by analysing 21 Si IV doublets observed towards 8 QSOs with Keck/HIRES. We found a weighted mean

$$\lambda = (0.5 \pm 1.3) \times 10^{-5} \quad (2)$$

The systematic error due to uncertainties in the Griesmann & Kling (2000) Si IV laboratory wavelengths is 0.2×10^{-5} . Recently, Bahcall, Steinhardt & Schlegel (2003) analysed 44 [O III] doublet QSO emission lines from the Sloan Digital Sky Survey Early Data Release (Schneider et al. 2002). Their constraint, $\lambda = (2 \pm 12) \times 10^{-5}$, is an order of magnitude weaker than equation 2. However, if one allows or expects spatial variations in λ , such a simplistic comparison is difficult since the two results constrain λ in very different environments (i.e. QSO emission regions and intervening absorption clouds).

1.1.2 The many-multiplet (MM) method

The many-multiplet (MM) method was introduced in Dzuba et al. (1999b) and Webb et al. (1999) as a generalisation of the AD method. The MM method constrains changes in λ by utilizing many observed transitions from different multiplets and different ions associated with each QSO absorption system. The full details behind this technique are presented in Dzuba et al. (1999a, 2001b, 2002). We presented a summary in M01a and listed the many important advantages the MM method holds over the AD method, including an effective order-of-magnitude precision gain. Therefore, we only outline the salient features of the method below.

For small shifts in λ (i.e. $\lambda = 1$), the rest wavenumber, λ_0 , of a transition with a measured redshift, z , in a QSO spectrum, can be written as

$$\lambda_z = \lambda_0 + q_1 x_z + q_2 y_z \quad (3)$$

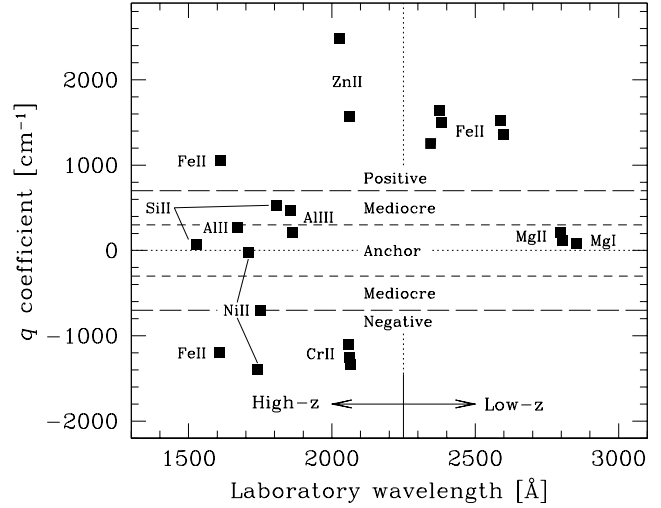


Figure 1. The distribution of q coefficients in (rest) wavelength space for the low- and high- z samples. Note the simple arrangement for the low- z Mg/Fe II systems: the Mg transitions are used as anchors against which the large, positive shifts in the Fe II transitions can be measured. Compare this with the complex arrangement for the high- z systems: low-order distortions of the wavelength scale will have a varied and complex effect on λ depending on which transitions are fitted in a given absorption system. In general, the complexity at high- z will yield more robust values of λ . For the discussion in Sections 5.7.2 and 5.7.3 we define several different ‘ q -types’ as follows: positive-shifters ($q > 700 \text{ cm}^{-1}$), negative-shifters ($q < -700 \text{ cm}^{-1}$), anchors ($300 < q < 700 \text{ cm}^{-1}$) and mediocre-shifters ($300 < q < 600 \text{ cm}^{-1}$).

where λ_0 is the wavenumber measured in the laboratory². If $z \ll 1$ then

$$x_z = \frac{z}{\lambda_0} \ll 1 \quad \text{and} \quad y_z = \frac{z^2}{\lambda_0^2} \ll 1 \quad (4)$$

are non-zero and the magnitude and sign of q_1 and q_2 determine the shift in the transition wavenumber. Since we only consider $\lambda = 1$, we may write

$$\lambda_z = \lambda_0 + q x_z \quad (5)$$

where we consolidate q_1 and q_2 into $q = q_1 + 2q_2$. The q coefficient represents all the relativistic corrections for the transition of interest and varies both in magnitude and sign from transition to transition. That is, if $\lambda \neq 0$, the QSO absorption lines will be shifted in a distinct pattern with respect to their laboratory values.

Fig. 1 illustrates the distribution of q coefficients for the different transitions used in the MM method. The q coefficients are calculated in Dzuba et al. (1999a, 2001a,b, 2002) using many-body techniques to include all dominant relativistic effects. The values used in the present study are listed in Table 2. The uncertainties in q are typically $\pm 30 \text{ cm}^{-1}$ for the Mg, Si, Al and Zn transitions but are $\pm 300 \text{ cm}^{-1}$ for those of Cr, Fe and Ni due to the more complicated electronic configurations involved. However, it is important to note that, in the absence of systematic effects in the QSO spectra, the form of equation 5 ensures that errors in the q coefficients can not lead to a non-zero λ .

² This equation does not strictly hold where level pseudocrossing occurs (Dzuba et al. 2001b, 2002). However, even in these cases, only the derivative of λ with respect to λ_0 is required for $\lambda = 10^{-3}$ (i.e. for λ_z sufficiently close to λ_0).

Webb et al. (1999) first applied the MM method to 30 Keck/HIRES QSO absorption systems (towards 14 QSOs) in the absorption redshift range $0.5 < z_{\text{abs}} < 1.6$, fitting only the transitions of Mg I, Mg II and Fe II. The large positive α coefficients for the Fe II transitions are in sharp contrast to the small values for the Mg transitions (Fig. 1): the Mg lines act as anchors against which the large shifts in the Fe II lines can be used to constrain α . The difference in α values ($\alpha \approx 1200 \text{ cm}^{-1}$) is much larger than for the Si IV transitions in the AD method ($\alpha \approx 500 \text{ cm}^{-1}$, Murphy et al. 2001c) and so the MM method allows significantly increased precision. Additionally, analysing the 5 Fe II and 3 Mg transitions allows a statistical gain over the AD method. Webb et al. (1999) explicitly demonstrated this increased precision, obtaining tentative evidence for a smaller α in the absorption clouds:

$$\alpha = (1.09 \pm 0.36) \times 10^5.$$

In M01a we analysed 18 independent Keck/HIRES absorption systems in the range $1.8 < z_{\text{abs}} < 3.5$. At these higher redshifts, shorter (rest) wavelength transitions are shifted into the optical bandpass. Fig. 1 shows the range of α coefficients available and their complex arrangement compared to the low- z Mg/Fe II systems. Such an arrangement should provide more robust estimates of α since any systematic effects in the QSO spectra will have a different effect on systems containing different transitions. Despite this, the high- z sample also yielded evidence for a smaller α in the past, consistent with the low- z systems. Combining this with a re-analysis of the Webb et al. (1999) data and including 3 low- z Mg/Fe II systems from the new data, we found 4.1 σ evidence for a variable α with 49 absorption systems over the range $0.5 < z_{\text{abs}} < 3.5$:

$$\alpha = (0.72 \pm 0.18) \times 10^5. \quad (6)$$

Such a potentially fundamental result requires extreme scrutiny and warrants a thorough examination of possible systematic errors. We carried out a detailed search for both instrumental and astrophysical systematic effects in M01b but were unable to identify any which explained the result in equation 6. Upper limits were placed on potential effects from atmospheric dispersion and possible isotopic abundance evolution but we indicated that further exploration of these possibilities was required.

In the present work we analyse a new, large sample of Keck/HIRES absorption systems using the MM method. We also re-analyse the previous datasets and significantly improve the analysis of potential systematic errors.

2 NEW AND PREVIOUS DATA

2.1 Keck/HIRES QSO spectra

The QSO observations were carried out by three independent groups, all using the high resolution spectrograph (HIRES, Vogt et al. 1994) on the Keck I 10-m telescope on Mauna Kea, Hawaii. We previously studied the first two samples in M01a and we outline changes and additions to these samples in Section 2.1.1 below. The new, large sample of 78 absorption systems is described in Section 2.1.2. Combining all three samples gives a total of 128 absorption systems observed towards 68 different QSOs. 8 absorption systems (towards 8 QSOs) were observed by two different groups, bringing the total number of independent Keck/HIRES spectra to 76. The absorption redshifts cover the range $0.2 < z_{\text{abs}} < 3.7$.

2.1.1 Previous low- and high- z samples

In M01a we analysed two independent Keck/HIRES datasets, termed the low- and high-redshift samples. The previous low- z sample was provided by C. W. Churchill and comprises 27 Mg/Fe II absorption systems in the spectra of 16 QSOs covering a redshift range $0.5 < z_{\text{abs}} < 1.8$ (e.g. Churchill et al. 2000a). An additional $z_{\text{abs}} = 1.4342$ system was contributed by Lu et al. (1996) but these data have been re-reduced and are now included in the new sample. The previous high- z sample was provided by J. X. Prochaska & A. M. Wolfe and comprises 11 QSO spectra which contain 17 damped Lyman- α systems (DLAs) in the range $1.8 < z_{\text{abs}} < 3.5$ and 3 lower redshift Mg/Fe II systems (Prochaska & Wolfe 1999). An additional DLA at $z_{\text{abs}} = 2.625$ was contributed by Outram, Chaffee & Carswell (1999). In the present work we add 2 further DLAs, again provided by J. X. Prochaska & A. M. Wolfe, bringing the total number of systems in the previous high- z sample to 23. Details of the data reduction for these previous samples are provided in M01a. We have reanalysed these samples (Section 3) in a way consistent with the new, larger dataset described in the next section.

2.1.2 The new sample

The main improvement on our previous results is due to a new dataset kindly provided by W. L. W. Sargent. The observations were carried out during numerous observing runs from 1993 November to 1999 November. The spectral resolution for most spectra was $\text{FWHM} \approx 6.6 \text{ km s}^{-1}$ ($R \approx 45000$). All spectra were reduced with the MAKEE³ package written by T. Barlow. QSO exposure times ranged from 1000–6000 s depending on the QSO magnitude and between 3–16 separate exposures were combined to form the final spectrum.

Thorium–argon (ThAr) emission lamp spectra, taken both before and after the QSO exposures, were used to calibrate the wavelength scale. MAKEE uses an internal list of ThAr air wavelengths derived using the Edlen (1966) formula from the measured vacuum thorium atlas of Palmer & Engleman (1983) and the argon atlas of Norlén (1973). MAKEE then converts the final wavelength scale to vacuum wavelengths using the Cauchy formula from Weast (1979) and not the (inverse of the) Edlen formula. As we noted in M01b, this distortion of the wavelength scale could lead to systematically non-zero values of α . For example, the effect on a $z_{\text{abs}} = 1.0$ Mg/Fe II system would be a spurious $\alpha = 0.25 \times 10^5$. We have corrected the wavelength scales of the reduced spectra to avoid such a distortion (see M01b for details). We test the accuracy of this wavelength scale in Section 5.3. The effect of slight miscalibrations (if any are present) on the overall α values is found to be negligible.

For each QSO spectrum we identified all absorption systems which contained enough MM transitions to yield meaningful constraints on α . We selected 500 km s^{-1} sections around each transition and defined a continuum by fitting a Legendre polynomial. 1 σ error arrays were generated assuming Poisson counting statistics. The average S/N per pixel for these spectral regions of interest ranged from 4–240, with most sections having $\text{S/N} \approx 30$ (see Fig. 2).

The new sample comprises 78 absorption systems, observed towards 46 QSOs, covering a wide redshift range, $0.2 < z_{\text{abs}} <$

³ See <http://www2.keck.hawaii.edu:3636/inst/hires/makeewww>.

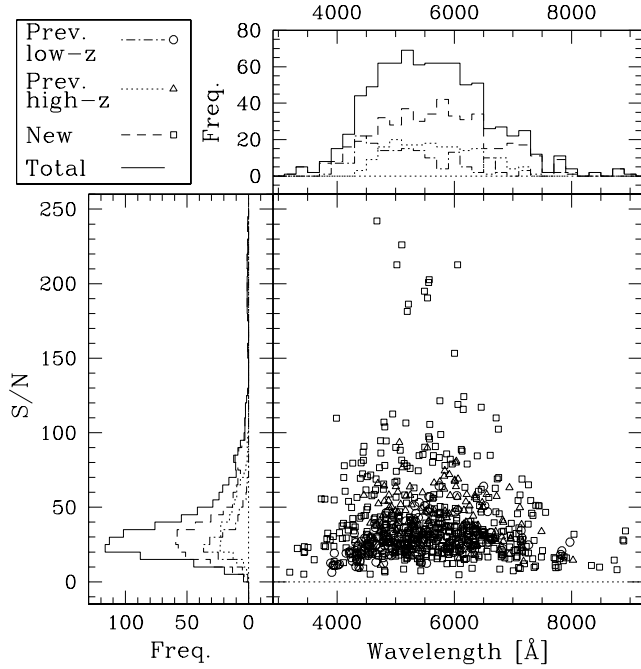


Figure 2. The distribution of S/N and central wavelength for the spectral regions of interest in the previous low- z , previous high- z and new samples.

3:7. Like the previous samples, the new sample conveniently divides into low- z ($z_{\text{abs}} < 1.8$) and high- z ($z_{\text{abs}} > 1.8$) subsamples. Table 1 shows the number of times each transition is used in the different subsamples. Mg/Fe II systems dominate the low- z region: 35 out of the 44 systems below $z_{\text{abs}} = 1.8$ contain only Fe II and Mg I or II, and, out of the remaining 9, only 1 system does not contain transitions of these ions. We provide an example Mg/Fe II absorption system, together with our Voigt profile fit, in Fig. 3. Note that fitting a large number of transitions allows the velocity structure of the absorption system to be reliably determined. This is further facilitated by the range in Fe II oscillator strengths and the presence of the weak Mg I line. The high- z systems are characterized by a diverse range of transitions from different ionic species. Table 1 shows that the strong Si II 1526, Al II 1670 and Fe II 1608 transitions are the most common. Fig. 4 illustrates a particularly high column density absorber which contains the lower abundance species, Cr II, Ni II and Zn II. Theoretically, the large magnitude of the q coefficients for the transitions of these species makes them very important for constraining β (see Fig. 1). However, since their optical depths are typically < 0.3 and since they are not detected in all high- z systems, their influence over β is reduced.

2.2 Atomic data

We summarize all relevant atomic data for the MM transitions of interest in Table 2. This is an updated version of table 1 in M01a, the main changes being the following:

(i) q coefficients. As noted in Section 1.1, the q_1 and q_2 coefficients used in previous works are now replaced by a single value, $q = q_1 + 2q_2$. The values of q for Mg I and Mg II are taken from Dzuba et al. (1999a,b) and those for Al II and Al III are from Dzuba et al. (2001b). All other q coefficients are from updated calculations of the type detailed in Dzuba et al. (2002). Conservative uncertainties are estimated by comparing other calculated quantities

Table 1. The frequency of occurrence for each transition in the different samples of QSO absorbers. For the new sample, we define low- z as $z_{\text{abs}} < 1.8$ and high- z as $z_{\text{abs}} > 1.8$. The previous low- z sample adheres to this definition but the previous high- z sample does contain 3 low- z systems. The low- z samples are dominated by the Mg/Fe II transitions. The high- z systems contain a diverse range of transitions and species but the strong Si II 1526, Al II 1670 and Fe II 1608 transitions are the most common.

Transition	Frequency of occurrence						Total
	low- <i>z</i> samples			high- <i>z</i> samples			
	Prev.	New	Tot.	Prev.	New	Tot.	
Mg I 2852	6	21	27	1	0	1	28
Mg II 2796	25	36	61	2	0	2	63
Mg II 2803	26	37	63	3	1	4	67
Al II 1670	0	5	5	11	30	41	46
Al III 1854	0	6	6	6	11	17	23
Al III 1862	0	6	6	4	9	13	19
Si II 1526	0	3	3	19	26	45	48
Si II 1808	0	3	3	15	8	23	26
Cr II 2056	0	2	2	9	7	16	18
Cr II 2062	0	1	1	10	7	17	18
Cr II 2066	0	0	0	8	7	15	15
Fe II 1608	0	4	4	19	28	47	51
Fe II 1611	0	1	1	9	6	15	16
Fe II 2344	21	26	47	5	7	12	59
Fe II 2374	10	20	30	3	2	5	35
Fe II 2382	22	34	56	3	5	8	64
Fe II 2587	20	34	54	3	3	6	60
Fe II 2600	25	36	61	3	3	6	67
Ni II 1709	0	0	0	7	7	14	14
Ni II 1741	0	1	1	12	6	18	19
Ni II 1751	0	1	1	12	8	20	21
Zn II 2026	0	1	1	7	6	13	14
Zn II 2062	0	1	1	7	6	13	14

(e.g. energy intervals, g -factors) with their experimental values and by comparing the results of several different calculation techniques. Thus, the errors quoted in Table 2 should be reliable but should not be treated as statistical.

Of particular note are large changes to the q coefficients for the Fe II 1608 and Ni II lines. The q coefficient used in M01a for Fe II 1608 was $q = 1002 \text{ cm}^{-1}$ but this was based on an incorrect excited state electronic configuration reported in Moore (1971), $3d^6 4p \text{ } ^6\text{P}_{7=2}^{\circ}$. The configuration shown in Table 2 is taken from Dzuba et al. (2002) who also calculate the new q coefficient, $q = 1200 \text{ cm}^{-1}$. Since Fe II 1608 is prominent in the high- z systems (see Table 1), this change has an important effect on the values of β in the previous high- z sample. We discuss this in detail in Section 4. The smaller changes to the Ni II q coefficients are due to the complicated electronic configuration of Ni II (Dzuba et al. 2001b, 2002). In this case, however, the effect on the values of β in the previous high- z sample is very small since the Ni II transitions are weak and only appear in ~ 25 per cent of our high- z systems (see Table 1).

(ii) Oscillator strengths. In order that the parameters derived from our Voigt profile fits to the QSO data can be compared with those of other studies, we have used the set of oscillator strengths recommended in the DLA database⁴ of Prochaska et al. (2001) (and

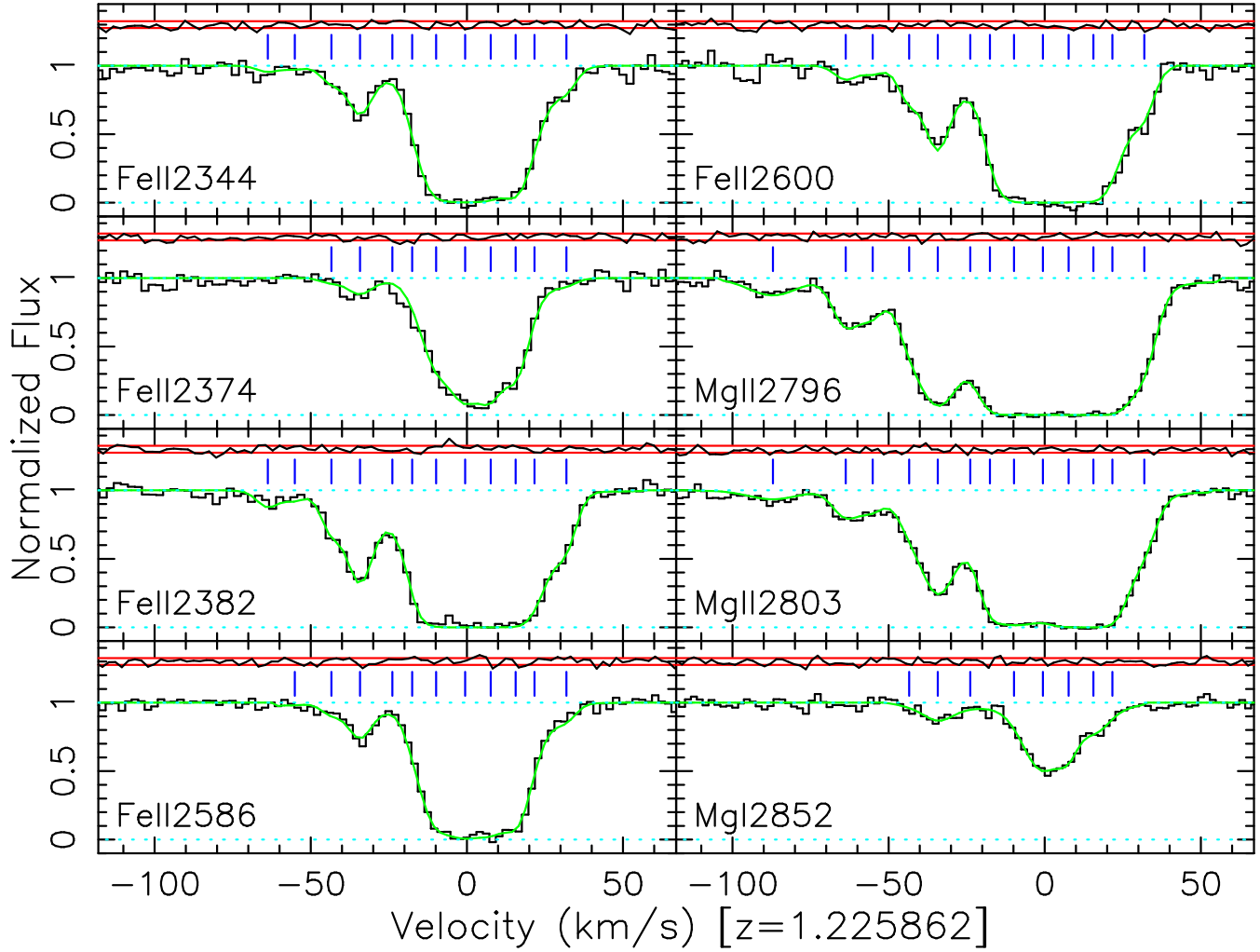
Q1437+3007, $z_{\text{em}}=3.00$, $z_{\text{abs}}=1.2259$ 

Figure 3. Mg/Fe II absorption system towards Q1437+3007 at $z_{\text{abs}} = 1.2259$. The data have been normalized by a fit to the continuum and plotted as a histogram. Our Voigt profile fit (solid curve) and the residuals (i.e. $[\text{data}] - [\text{fit}]$), normalized to the 1σ errors (horizontal solid lines), are also shown. The tick-marks above the continuum indicate individual velocity components. Note the range of line strengths in Fe II, facilitating determination of the velocity structure. The large number of Fe II transitions and the large number of velocity components allows for tight constraints to be placed on z_{abs} . The Mg II 2852 and Fe II 2374 transitions allow $z_{\text{abs}} = 1.2259$ to be constrained by the velocity 0 km s^{-1} components whereas the Mg II and remaining Fe II transitions constrain $z_{\text{abs}} = 1.2259$ with the velocity 35 km s^{-1} component.

references therein). These changes have a negligible effect on our values of $\alpha = 0.0$.

(iii) Al III hyperfine structure. In M01a we used composite wavelengths to fit the Al III profiles. However, Griesmann & Kling (2000) clearly resolved the hyperfine components in their laboratory Fourier transform spectra (FTS) and found that the hyperfine splitting is 2.5 km s^{-1} , comparable with the resolution of Keck/HIRES. In M01b we found that the composite values were adequate for our previous high- z sample, primarily because Al III only appeared in 6 absorption systems. However, we now include the Al III hyperfine components listed in Table 2 in our Voigt profile fits to the previous and new samples.

Aside from Al, all the elements in Table 2 have several naturally occurring isotopes and so each QSO absorption line will be a blend of absorption lines from each isotopic component. However, the isotopic structures are only known for the transitions of Mg I (Hallstadius 1979) and Mg II (Drullinger, Wineland & Bergquist 1980). The latter authors also determined the hyperfine splitting constant for the Mg II transitions. Pickering et al. (1998) used laboratory FTS to derive the wavelengths of the individual isotopes and main hyperfine components for these transitions and these are the values given in Table 2.

In M01a we estimated the isotopic structures for the two Si II transitions by scaling the isotopic shifts for Mg II 2796 by the mass shift,

$$\Delta \lambda_i / \Delta \lambda_0 = m^{-2}; \quad (7)$$

for $\Delta \lambda_i$ the shift in wavenumber for isotope i where m is the atomic mass. We give these estimated isotopic structures in Table

⁴ Available at <http://kingpin.ucsd.edu/~hiresdla>.

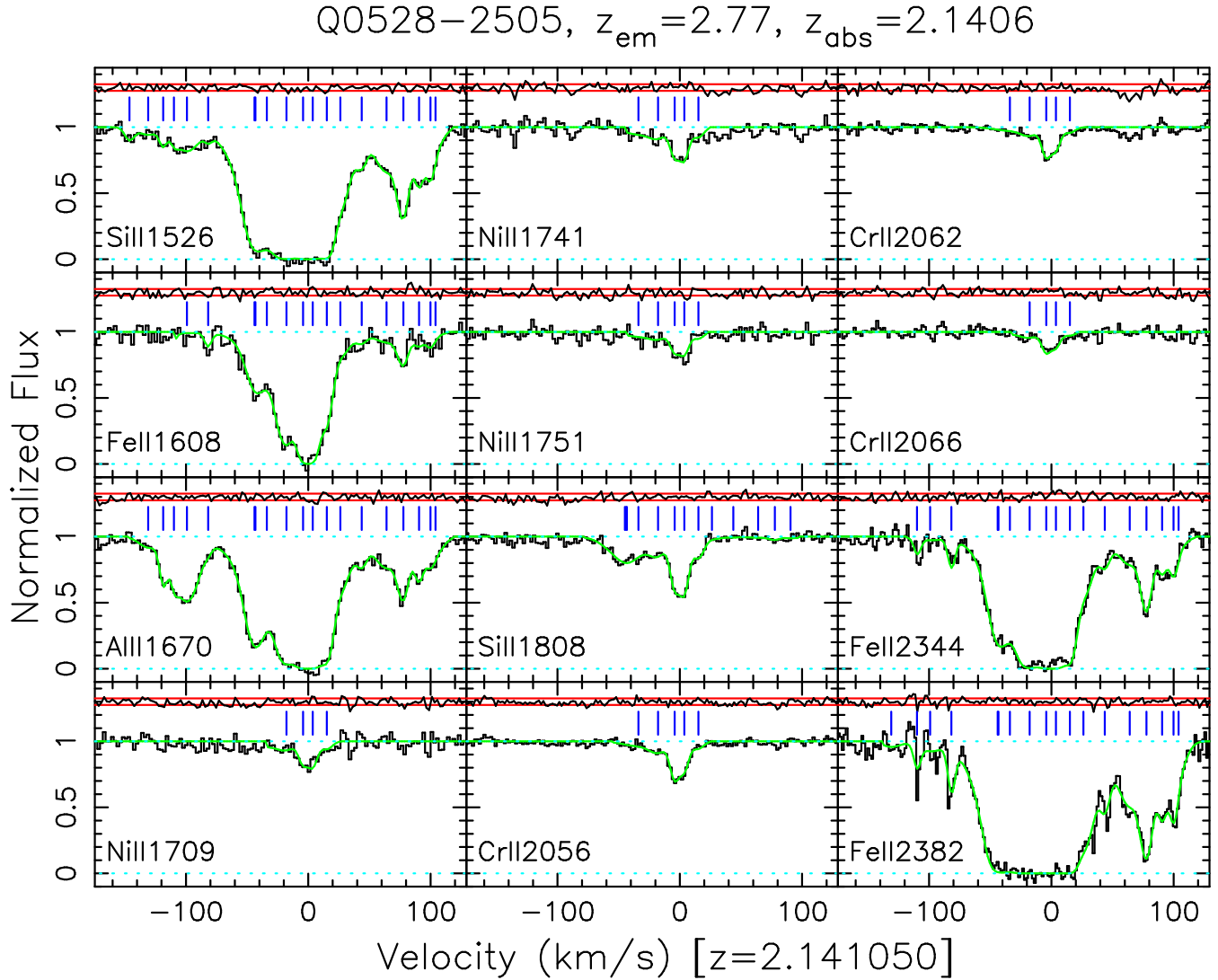


Figure 4. Heavy element absorption lines in the damped Lyman- α system towards Q0528–2505 at $z_{\text{abs}} = 2.1406$. The data have been normalized by a fit to the continuum and plotted as a histogram. Our Voigt profile fit (solid curve) and the residuals (i.e. $[data] - [fit]$), normalized to the 1σ errors (horizontal solid lines), are also shown. The tick-marks above the continuum indicate individual velocity components. Note the large range in line strengths for the different transitions. The velocity structure is well-constrained by Si II 1526, Al II 1670 and Fe II 1608 while the Ni II and Cr II transitions are strong enough to constrain $\tau = 0$ with the velocity 0 km s^{-1} components. This system is at low enough redshift for the Fe II 2344 and 2382 transitions to be detected. These combine with Si II 1526, Al II 1670 and Fe II 1608 to constrain $\tau = 0$ with the components at velocity 80 km s^{-1} .

2. Our approximation may break down if the *specific* isotopic shifts for the Si II transitions are very different to those of Mg II 2796. Very recent theoretical calculations (Berengut, Dzuba & Flambaum 2003) suggest that these are of opposite sign to the normal mass shift and so the shifts in Table 2 are probably overestimates. We discuss the effect this may have on our values of $\tau = 0$ in Section 5.5.

At the time of our calculations, no measurements or theoretical estimates of the isotopic structures existed for the other transitions (to our knowledge) and so we used the composite values listed in Table 2. Since that time, measurements (Matsubara et al. 2002) and theoretical estimates (Berengut et al. 2003) of the Zn II isotopic structure have become available. In Section 5.5 we discuss the potential effects of differential isotopic saturation and strong cosmological evolution of the isotopic abundances on our values of $\tau = 0$.

Finally, we note that the Whaling et al. (1995) Ar II wavenumbers used to calibrate the Si II, Al II and Al III wavelengths are systematically larger than those of Norlén (1973) used to calibrate the wavelengths of the remaining lines. The difference between the calibration scales is proportional to the wavenumber: $\Delta \lambda / \lambda = 7 \times 10^{-8}$. In M01b we note that calibration errors of this type will be absorbed by the redshift parameters of the QSO absorption lines and so, as long as all laboratory wavelengths are normalized to the one calibration scale, values of $\tau = 0$ will be unaffected. We have therefore normalized all laboratory wavelengths in Table 2 to the Norlén (1973) calibration scale.

3 ANALYSIS

We have detailed our analysis procedure in M01a and so only provide a short summary here. For each absorption system we con-

Table 2. Atomic data for the MM transitions in our analysis. Information for isotopic and hyperfine components is given in italics. Column 2 shows the mass number, A , for each species. The origin of the laboratory wavenumbers (cm^{-1}) and wavelengths (\AA) is summarized in M01a. Columns 5 and 6 show the updated ground and excited state electronic configurations. The ID letters in column 7 are used in Table 3 to indicate the transitions used in our fits to each absorption system. Column 8 shows the ionization potential for the relevant ion, IP^+ , and for the ion with a unit lower charge, IP . Column 9 shows the oscillator strengths, f , from the DLA database⁴ of Prochaska et al. (2001) or the relative strengths of the isotopic (Rosman & Taylor 1998) or hyperfine components (italics). The q coefficients are from Dzuba et al. (1999a,b, 2001b, 2002) and the uncertainties are discussed in the text. The Si II, Al II and Al III wavenumbers have been scaled from their literature values due to the Norlén/Whaling et al. calibration difference.

Ion	A	λ_0 (\AA)	ν_0 (cm^{-1})	Ground	Upper	ID	IP, IP^+ (eV)	f or %	q (cm^{-1})
Mg I	24.32	2852.96310(8)	35051.277(1) ^a	$3s^2\ ^1S_0$	$3s3p\ ^1P_1$	a	—, 7.7	1.81	86(10)
	26	2852.95977	35051.318 ^a					11.0	
	25	2852.96316	35051.295 ^a					10.0	
	24	2852.96359	35051.271 ^a					79.0	
Mg II	24.32	2796.3543(2)	35760.848(2) ^a	$3s^2\ S_{1=2}$	$3p^2\ P_{3=2}$	b	7.7, 15.0	0.6123	211(10)
	26	2796.3473	35760.937 ^a					11.0	
	25	2796.3492	35760.913 ^a					5.8	
	25	2796.3539	35760.853 ^a					4.2	
	24	2796.3553	35760.835 ^a					79.0	
		2803.5315(2)	35669.298(2) ^a	$3s^2\ S_{1=2}$	$3p^2\ P_{1=2}$	c		0.3054	120(10)
	26	2803.5244	35669.388 ^a					11.0	
	25	2803.5258	35669.370 ^a					3.0	
	25	2803.5266	35669.360 ^a					2.8	
	25	2803.5305	35669.310 ^a					1.5	
	25	2803.5313	35669.300 ^a					2.7	
	24	2803.5324	35669.286 ^a					79.0	
Al II	27.00	1670.7887(1)	59851.972(4) ^b	$3s^2\ ^1S_0$	$3s3p\ ^1P_1$	d	6.0, 18.9	1.88	270(30)
Al III	27.00	1854.71841(3)	53916.540(1) ^b	$3s^2\ S_{1=2}$	$3p^2\ P_{3=2}$	e	18.9, 28.4	0.539	464(30)
		1854.70910(3)	53916.8111(8) ^b					41.7	
		1854.72483(2)	53916.3536(6) ^b					58.3	
		1862.79126(7)	53682.880(2) ^b	$3s^2\ S_{1=2}$	$3p^2\ P_{1=2}$	f		0.268	216(30)
		1862.78046(5)	53683.1915(15) ^b					41.7	
		1862.79871(4)	53682.6654(12) ^b					58.3	
Si II	28.11	1526.70709(2)	65500.4492(7) ^b	$3s^2\ 3p^2\ P_{1=2}^o$	$3s^2\ 4s^2\ S_{1=2}$	g	8.2, 16.3	0.127	68(30)
	30	1526.7040	65500.583					3.1	
	29	1526.7055	65500.517					4.7	
	28	1526.7073	65500.442					92.2	
		1808.01301(1)	55309.3365(4) ^b	$3s^2\ 3p^2\ ^2D_{3=2}$	$3s^2\ 3p^2\ ^2D_{3=2}$	h		0.00218	531(30)
	30	1808.0094	55309.446					3.1	
	29	1808.0113	55309.390					4.7	
	28	1808.0132	55309.330					92.2	
Cr II	52.06	2056.25693(8)	48632.055(2) ^c	$3d^5\ ^6S_{5=2}$	$3d^4\ 4p\ ^6P_{7=2}^o$	i	6.8, 16.5	0.105	1107(150)
		2062.23610(8)	48491.053(2) ^c		$3d^4\ 4p\ ^6P_{5=2}^o$	j		0.078	1251(150)
		2066.16403(8)	48398.868(2) ^c		$3d^4\ 4p\ ^6P_{3=2}^o$	k		0.0515	1334(150)
Fe II	55.91	1608.45085(8)	62171.625(3) ^d	$3d^6\ 4s\ a^6D_{9=2}$	$3d^5\ 4s4p\ ^6P_{7=2}^o$	l	7.9, 16.2	0.0580	1200(300)
		1611.20034(8)	62065.528(3) ^d		$3d^6\ 4p\ ^4F_{7=2}^o$	m		0.00136	1050(300)
		2344.2130(1)	42658.2404(2) ^e		$3d^6\ 4p\ ^6P_{7=2}^o$	n		0.114	1254(150)
		2374.4603(1)	42114.8329(2) ^e		$3d^6\ 4p\ ^6F_{9=2}^o$	o		0.0313	1640(150)
		2382.7642(1)	41968.0642(2) ^e		$3d^6\ 4p\ ^6F_{11=2}^o$	p		0.320	1498(150)
		2586.6496(1)	38660.0494(2) ^e		$3d^6\ 4p\ ^6D_{7=2}^o$	q		0.06918	1520(150)
		2600.1725(1)	38458.9871(2) ^e		$3d^6\ 4p\ ^6D_{9=2}^o$	r		0.23878	1356(150)
Ni II	58.76	1709.6042(1)	58493.071(4) ^c	$3d^9\ ^2D_{5=2}$	$3d^8\ 4p\ ^2F_{5=2}^o$	s	7.6, 18.2	0.0324	20(250)
		1741.5531(1)	57420.013(4) ^c		$3d^8\ 4p\ ^2D_{5=2}^o$	t		0.0427	1400(250)
		1751.9157(1)	57080.373(4) ^c		$3d^8\ 4p\ ^2F_{7=2}^o$	u		0.0277	700(250)
Zn II	65.47	2026.13709(8)	49355.002(2) ^c	$3d^{10}\ 4s^2\ S_{1=2}$	$3d^{10}\ 4p\ ^2P_{3=2}^o$	v	9.4, 17.8	0.489	2479(25)
		2062.66045(9)	48481.077(2) ^c		$3d^{10}\ 4p\ ^2P_{1=2}^o$	w		0.256	1577(25)

^aPickering, Thorne & Webb (1998); ^bGriesmann & Kling (2000); ^cPickering et al. (2000); ^dPickering et al. (2002); ^eNave et al. (1991).

struct multiple velocity component Voigt profile fits to the data using VPFIT (v5)⁵. Each velocity component is described by three parameters: the column density, the Doppler width or b parameter and the redshift, z_{abs} , of the absorbing gas. We have modified VPFIT to include β as a free parameter: for each transition we alter the rest wavelength using equation 5 so that all velocity components shift in concert. To constrain $\beta = 1$ one must tie together the z_{abs} parameters of the corresponding velocity components in different transitions. This assumes negligible proper motion between the absorbing gas of different ionic species. We discuss this assumption in detail in Section 5.1.

We minimize χ^2 simultaneously for all fitted transitions to find the best fitting value of β . Parameter errors are calculated from the diagonal terms of the final parameter covariance matrix (Fisher 1958). We have performed Monte Carlo simulations of absorption systems of varying complexity (i.e. different numbers of velocity components and transitions fitted) and with a range of input values of β to verify that VPFIT returns the correct values and 1σ errors (see also Section 5.7).

We impose two self-consistency checks on each absorption system before accepting a value of β . Firstly, we require the value of χ^2 per degree of freedom, χ^2_{dof} , to be < 1 . Secondly, we construct two fits to the data with different constraints on the b parameters: (i) entirely thermal broadening and (ii) entirely turbulent broadening⁶. We require that the values of β derived from both fits be consistent with each other since the choice above should not greatly affect β (i.e. the measured position of velocity components should not change systematically). We rejected only 4 systems in this way.

4 RESULTS

4.1 Raw QSO results

We present the χ^2 minimization results in Table 3 for the previous and new samples separately. We list the QSO (B1950) name, the emission redshift, z_{em} , the nominal absorption redshift, z_{abs} , and β for each absorption system with the associated 1σ statistical error. The transitions fitted in each system are indicated with the ID letters defined in Table 2. We present basic statistics for the different samples in Table 4: $\bar{h} = \bar{h}_w$ is the weighted mean with 1σ error, $\bar{h} = \bar{h}_u$ is the unweighted mean, S_0 is the significance of the departure of the weighted mean from zero, rms is the root-mean-square deviation from the mean of β , $\bar{h}(\pm 1\sigma)$ is the mean 1σ error and χ^2_{dof} is the value of χ^2 per degree of freedom with $\bar{h} = \bar{h}_w$ as the model.

The statistics in Table 4 indicate a smaller β over the redshift range $0.2 < z_{\text{abs}} < 3.7$ at the 5.6% significance level:

$$\beta = (0.574 \pm 0.102) \times 10^{-5} \quad (8)$$

We note the consistency between the previous low- z , previous high- z and new samples. Breaking the new sample down into low- z ($z_{\text{abs}} < 1.8$) and high- z ($z_{\text{abs}} > 1.8$) subsamples also yields

Table 3. The raw results from the χ^2 minimization procedure. For each absorption system we list the QSO emission redshift, z_{em} , the nominal absorption system redshift, z_{abs} , the transitions fitted and the value of β with associated 1σ statistical error. A ‘**’ after β indicates systems included in the ‘high-contrast’ sample. An additional random error of 2.09×10^{-5} should be added in quadrature to these systems to form the fiducial sample (see Section 4.2).

Object	z_{em}	z_{abs}	Transitions ^a	β	1σ (10 ⁻⁵)
Previous low- z sample					
0002+ 0507	1.90	0.85118	bcnopqr	0.346	1.279
0117+ 2118	1.49	0.72913	abcqr	0.084	1.297
		1.0479	bcnpr	0.223	2.200
		1.3246	bcpqr	0.695	0.803
		1.3428	cnpq	1.290	0.948
0420 0127	0.915	0.63308	abcr	4.211	4.076
0450 1312	2.25	1.1743	bnopr	3.070	1.098
		1.2294	bcnpqr	1.472	0.836
		1.2324	bcp	1.017	2.752
0454+ 0356	1.34	0.85929	acnoprq	0.405	1.325
		1.1534	bcnqr	0.749	1.782
0823 2220	0.91	0.91059	bcnpqr	0.394	0.609
1148+ 3842	1.30	0.55339	bcqr	1.861	1.716
1206+ 4557	1.16	0.92741	bcnopqr	0.218	1.389
1213 0017	2.69	1.3196	abcnopqr	0.738	0.760
		1.5541	bcnopqr	1.268	0.892
1222+ 2251	2.05	0.66802	bcnpr	0.067	1.474
1225+ 3145	2.22	1.7954	abcnopr	1.296	1.049
1248+ 4007	1.03	0.77292	bcnopqr	2.165	1.191
		0.85452	bcnpqr	0.021	1.268
1254+ 0443	1.02	0.51934	abcqr	3.371	3.247
		0.93426	bcnpqr	1.485	1.908
1317+ 2743	1.01	0.66004	bcnpqr	0.590	1.515
1421+ 3305	1.91	0.84324	bcnopqr	0.099	0.847
		0.90301	bcnopqr	0.998	1.783
		1.1726	bcnpr	2.844	1.448
1634+ 7037	1.34	0.99010	bcnpqr	1.094	2.459
Previous high- z sample					
0019 1522	4.53	3.4388	ghl	0.925	3.958
0100+ 1300	2.68	2.3095	efgklmvw	3.941	1.368
0149+ 3335	2.43	2.1408	defghijklmstu	5.112	2.118
0201+ 3634	2.49	1.4761	cnoqr	0.647	1.219
		1.9550	ehil	1.989	1.048
		2.3240	deghl	0.758	1.592
		2.4563	dgl	3.731	2.285
		2.4628	ghiltu	0.572	1.719
0347 3819	3.23	3.0247	gl	2.795	3.429
0841+ 1256	2.55	2.3742	dghijtuvw	2.277	3.816
		2.4761	dghijklmtu	4.304	1.944
1215+ 3322	2.61	1.9990	defghijlmstuvw	5.648	3.131
1759+ 7539	3.05	2.6253	eghklmstu	0.750	1.387
		2.6253 ^b	dglmtu	0.492	1.645
2206 1958	2.56	0.94841	bcnpqr	3.659	1.855
		1.0172	abcnopqr	0.322	0.732
		1.9204	dghijklmstuvw	1.878	0.702
2230+ 0232	2.15	1.8585	dghjlnpstu	5.407	1.179
		1.8640	ghijklmnostuvw	0.998	0.492
2231 0015	3.02	2.0653	ghjklmtuvw	2.604	1.015
2348 1444	2.94	2.2794	ghl	1.346	4.180
2359 0216	2.31	2.0951	dghijklstuvw	0.068	0.722
		2.1539	dfgl	4.346	3.338

⁵ Available at <http://www.ast.cam.ac.uk/~rfc/vpfit.html>

⁶ This is a minor departure from our previous analysis. In M01a we constructed a third fit for each absorption system where the thermal and turbulent component of the b parameters were determined by goodness of fit. Such a fit is more computationally intensive and, in general, the thermal and turbulent b parameters are poorly determined. In M01a we found that this fit did not lead to any inconsistent values of β and so fits (i) and (ii) provide a sufficient consistency check.

Table 3 – continued: The new sample.

Object	z_{em}	z_{abs}	Transitions ^a	$\Delta\alpha/\alpha$ (10^{-5})	
New sample					
0000 2620	4.11	1.4342	bcpr	1.256	1.167
		3.3897	dglm	7.666	3.231
0002+ 0507	1.90	0.59137	bcnpqr	3.100	2.428
		0.85118	efnopqr	0.494	1.021
0055 2659	3.66	1.2679	abcpqr	1.669	2.745
		1.3192	bcpqr	2.642	2.457
		1.5337	abcnopqr	1.319	1.072
0058+ 0155	1.96	0.61256	bcnopqr	0.374	1.189
		0.72508	bcnpqr	2.637	3.522
0119 0437	1.95	0.65741	bcnopqr	7.123	4.599
0153+ 7427	2.33	0.74550	bcnpqr	2.168	0.778
0207+ 0503	4.19	3.6663	dgl	0.748	3.468
0216+ 0803	2.99	1.7680	eflnopqr	0.044	1.235
0237 2321	2.23	1.3650	deghlnop	0.197	0.565
0241 0146	4.04	2.0994	dnop	0.739	2.675
0302 2223	1.41	1.0092	abcnopqr	0.189	1.008
0449 1325	3.09	1.2667	abcnopq	1.212	1.430
0528 2505	2.77	0.94398	bcr	0.759	2.335
		2.1406	dghijklnpstu	0.853	0.880
		2.8114	defghijklmstuvw	0.850	0.846
0636+ 6801	3.17	1.2938	bcpqr	1.392	0.623
0741+ 4741	3.21	1.6112	abcnpq	1.299	1.726
		3.0173	dghl	0.794	1.796
0757+ 5218	3.24	2.6021	defl	1.396	1.955
		2.8677	dgl	3.837	3.288
0841+ 1256	2.55	1.0981	bnopr	3.589	1.203
		1.1314	abcnpqr	0.562	0.787
		1.2189	abcnopqrvw	0.522	0.542
		2.3742	deghijknqrtuvw	1.435	1.227
0930+ 2858	3.42	3.2351	dgl	0.867	1.777
0940 1050	3.05	1.0598	abcnpqr	0.453	1.572
0956+ 1217	3.31	2.3103	defl	2.161	5.977
1009+ 2956	2.62	1.1117	bcnpqr	5.461	2.518
1011+ 4315	3.10	1.4162	bcnopqr	0.892	0.552
		2.9587	deghlmsu	2.475	1.706
1055+ 4611	4.12	3.3172	dgl	2.706	5.677
1107+ 4847	2.97	0.80757	abcpq	1.199	1.222
		0.86182	abcqr	2.030	1.632
		1.0158	abcp	2.086	0.934
1132+ 2243	2.88	2.1053	defgl	6.323	3.622
1202 0725	4.70	1.7549	bcqr	1.465	2.182
1206+ 4557	1.16	0.92741	abcnopqr	0.275	0.776
1223+ 1753	2.94	2.4653	hijkmsuvw	1.635	1.919
		2.5577	dglnp	0.546	1.199
1225+ 3145	2.22	1.7954	defghl	1.352	1.388
1244+ 3142	2.95	0.85048	bcpr	6.897	7.012
		2.7504	dgl	2.414	4.110
1307+ 4617	2.13	0.22909	abcr	2.551	5.392
1337+ 1121	2.97	2.7955	dhl	4.103	8.538
1425+ 6039	3.20	2.7698	dgl	0.688	1.843
		2.8268	dgl	0.433	0.827
1437+ 3007	3.00	1.2259	abcnopqr	0.308	1.460
1442+ 2931	2.76	2.4389	dgl	0.882	1.473
1549+ 1919	2.83	1.1425	cfnpqr	0.076	0.671
		1.3422	nopq	0.740	1.232
		1.8024	def	3.050	2.473
1626+ 6433	2.32	0.58596	bcr	1.977	4.529
		2.1102	defgl	0.705	1.068
1634+ 7037	1.34	0.99010	abcdnopqr	2.194	1.343
1850+ 4015	2.12	1.9900	ghijklmnopqrvw	1.663	0.859
1946+ 7658	3.02	1.7385	efhijmntu	0.212	1.857
		2.8433	dgl	4.743	1.289

Table 3 – continued: The new sample (continued).

Object	z_{em}	z_{abs}	Transitions ^a	$\Delta\alpha/\alpha$ (10^{-5})	
2145+ 0643	1.00	0.79026	bcnopqr	0.087	0.589
2206 1958	2.56	1.0172	abcqr	1.354	0.883
		2.0762	dl	1.429	3.022
2231 0015	3.02	1.2128	abcopqr	1.223	1.465
		2.0653	efghijklmstuvw	1.707	1.249
		2.6532	dglstu	3.348	1.904
2233+ 1310	3.30	2.5480	dgl	2.942	5.207
		2.5548	defgl	1.732	6.349
		3.1513	dgl	4.005	3.301
2343+ 1232	2.52	0.73117	abcoqr	1.211	0.975
		1.5899	acdefgqr	0.453	1.187
		2.1711	cdefnp	0.961	1.295
		2.4300	dghijklmstuvw	1.224	0.389
2344+ 1228	2.77	1.0465	abcinopqr	0.747	1.530
		1.1161	abcopqr	0.009	1.963
		2.5378	dgl	3.205	2.094

^aTransitions identified as in Table 2; ^bThis absorber contributed by Outram et al. (1999).

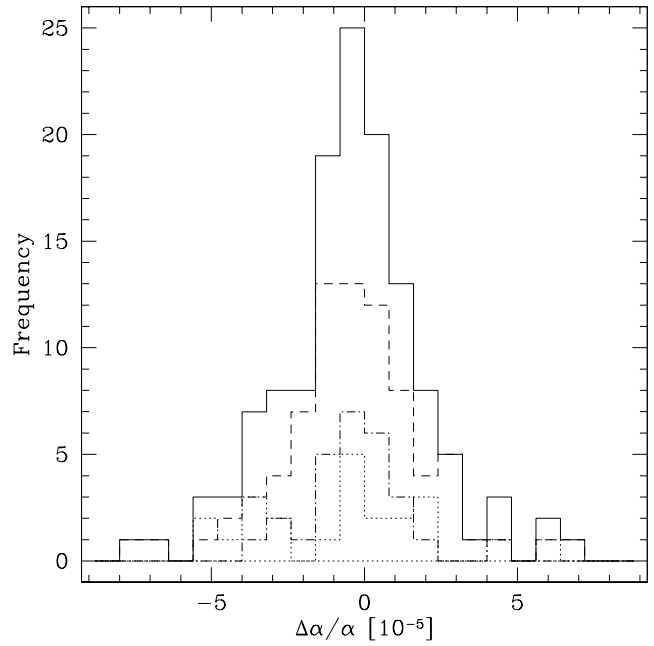


Figure 5. Histograms of raw results from Table 3. The distribution of $\Delta\alpha/\alpha$ for the previous low- z (dot-dashed line), previous high- z (dotted line) and new (dashed line) samples are shown together with the overall distribution (solid line, binned differently in Fig. 15a).

consistent results. We also see an overall agreement between the weighted and unweighted means, indicating that our results are not dominated by a small number of highly significant points. This is supported by the histogram in Fig. 5 which shows a symmetric, roughly Gaussian distribution for the values of $\Delta\alpha/\alpha$.

We illustrate the distribution of $\Delta\alpha/\alpha$ over redshift and cosmological time in Fig. 6. The upper panel shows the raw values of $\Delta\alpha/\alpha$ (with their 1 σ error bars) for each sample separately. The middle panel shows an arbitrary binning of each sample such that each bin has an equal number of points (aside from the highest z bin which also contains the remaining points after dividing the to-

Table 4. Statistics for the raw QSO results and tests for systematic errors. The previous samples are described in Section 2.1.1. For the new and total samples, ‘low- z ’ means $z_{\text{abs}} < 1.8$ and ‘high- z ’ means $z_{\text{abs}} > 1.8$. For each sample, $\langle z_{\text{abs}} \rangle$ is the mean absorption redshift, N_{abs} is the number of absorption systems, $\langle h \rangle = \langle i \rangle_w$ is the weighted mean, $\langle h \rangle = \langle i \rangle$ is the unweighted mean, S_0 is the significance of the weighted mean (with respect to zero), rms is the root-mean-square deviation from the mean, $\langle h \rangle - \langle i \rangle$ is the mean 1 σ error and χ^2 is χ^2 per degree of freedom using $\langle h \rangle = \langle i \rangle_w$ as the model.

Sample	$\langle z_{\text{abs}} \rangle$	N_{abs}	$\langle h \rangle = \langle i \rangle_w$	$\langle h \rangle = \langle i \rangle$	S_0	rms	$\langle h \rangle - \langle i \rangle$	χ^2
QSO results								
Raw results (Fig. 6)								
Prev. low- z	1.00	27	0:513 0:224	0:305 0:304	2.28	1.579	1:554 0:153	0.981
Prev. high- z	2.17	23	0:672 0:244	0:656 0:601	2.76	2.880	1:951 0:232	3.082
New low- z	1.11	44	0:537 0:159	0:652 0:321	3.37	2.131	1:757 0:204	1.123
New high- z	2.60	34	0:623 0:224	0:053 0:473	2.78	2.755	2:604 0:318	1.533
New total	1.76	78	0:566 0:130	0:391 0:276	4.36	2.441	2:126 0:186	1.284
low- z total	1.07	74	0:539 0:130	0:562 0:226	4.24	1.941	1:663 0:134	1.051
high- z total	2.50	54	0:637 0:172	0:227 0:389	3.72	2.862	2:400 0:224	2.179
Raw sample	1.67	128	0:574 0:102	0:421 0:210	5.62	2.379	1:974 0:127	1.515
Removing extra scatter at high- z (Figs. 7 and 8)								
High-contrast sample removed	2.65	32	0:518 0:347	0:011 0:517	1.49	2.926	3:070 0:308	1.207
High-contrast errors increased	2.50	54	0:563 0:291	0:227 0:389	1.94	2.862	2:881 0:191	1.103
All high- z errors increased	2.50	54	0:601 0:328	0:227 0:389	1.83	2.862	2:986 0:194	1.000
High- z -clip	2.54	44	0:489 0:191	0:273 0:341	2.57	2.261	2:559 0:263	0.997
Fiducial sample	1.67	128	0:543 0:116	0:421 0:210	4.66	2.379	2:177 0:124	1.065
Systematic error tests								
ThAr calibration test: $\langle \lambda \rangle = \langle \lambda \rangle_{\text{ThAr}}$ (Fig. 15)								
Prev. low- z	1.00	27	0:016 0:021	0:034 0:045	0.74	0.234	0:129 0:008	3.697
Prev. high- z	2.10	18	0:013 0:020	0:015 0:059	0.66	0.250	0:165 0:043	3.212
New low- z	1.14	41	0:008 0:014	0:003 0:036	0.59	0.229	0:123 0:016	3.095
New high- z	2.63	32	0:019 0:014	0:016 0:052	1.38	0.293	0:148 0:022	2.714
New total	1.79	73	0:006 0:010	0:005 0:030	0.57	0.259	0:134 0:013	2.915
low- z total	1.08	71	0:006 0:011	0:006 0:027	0.54	0.230	0:124 0:010	3.286
high- z total	2.52	47	0:014 0:012	0:013 0:041	1.24	0.284	0:159 0:022	2.827
Total	1.66	118	0:004 0:008	0:009 0:023	0.48	0.253	0:138 0:011	3.091
Composite wavelengths only: $\langle \lambda \rangle = \langle \lambda \rangle_{\text{comp}}$ (Fig. 16, top panel)								
Prev. low- z	1.00	27	0:802 0:227	0:557 0:334	3.54	1.736	1:567 0:156	1.094
Prev. high- z	2.17	23	0:736 0:243	0:731 0:608	3.03	2.918	1:929 0:230	3.178
New low- z	1.11	44	0:550 0:161	0:609 0:329	3.42	2.184	1:779 0:209	1.060
New high- z	2.60	34	0:650 0:224	0:085 0:456	2.90	2.660	2:636 0:326	1.457
New total	1.76	78	0:584 0:131	0:380 0:274	4.47	2.417	2:152 0:191	1.218
low- z total	1.07	74	0:650 0:128	0:648 0:238	5.08	2.045	1:681 0:138	1.098
high- z total	2.50	54	0:667 0:172	0:251 0:380	3.89	2.792	2:411 0:229	2.129
Total	1.67	128	0:656 0:103	0:481 0:212	6.39	2.397	1:989 0:129	1.520
Strong isotopes only: $\langle \lambda \rangle = \langle \lambda \rangle_{\text{iso}}$ (Fig. 16, middle panel)								
Prev. low- z	1.00	27	1:204 0:228	0:885 0:353	5.29	1.834	1:567 0:157	1.257
Prev. high- z	2.17	23	0:738 0:244	0:734 0:619	3.03	2.967	1:928 0:226	3.210
New low- z	1.11	44	0:860 0:159	0:834 0:323	5.40	2.145	1:768 0:206	1.279
New high- z	2.60	34	0:634 0:224	0:077 0:463	2.84	2.700	2:626 0:325	1.494
New total	1.76	78	0:784 0:130	0:504 0:275	6.04	2.432	2:142 0:190	1.363
low- z total	1.07	74	0:984 0:128	0:913 0:239	7.71	2.055	1:674 0:137	1.300
high- z total	2.50	54	0:638 0:171	0:231 0:384	3.72	2.824	2:404 0:228	2.143
Total	1.67	128	0:861 0:102	0:626 0:215	8.41	2.433	1:982 0:128	1.663
Atmospheric dispersion corrected: $\langle \lambda \rangle = \langle \lambda \rangle_{\text{adc}}$ (Fig. 17)								
Prev. low- z	1.00	27	0:098 0:225	0:142 0:339	0.43	1.762	1:554 0:153	1.208
Prev. high- z	2.17	23	0:637 0:244	0:668 0:583	2.61	2.794	1:951 0:232	2.979
New low- z	1.11	44	0:416 0:159	0:557 0:319	2.61	2.118	1:757 0:204	1.050
New high- z	2.60	34	0:740 0:224	0:189 0:472	3.31	2.755	2:604 0:318	1.545
New total	1.76	78	0:525 0:130	0:397 0:274	4.48	2.423	2:126 0:186	1.266
low- z total	1.07	74	0:288 0:127	0:309 0:232	2.27	1.999	1:663 0:134	1.118
high- z total	2.50	54	0:764 0:172	0:363 0:386	4.45	2.837	2:400 0:224	2.099
Total	1.67	128	0:457 0:102	0:332 0:211	4.48	2.389	1:974 0:127	1.558

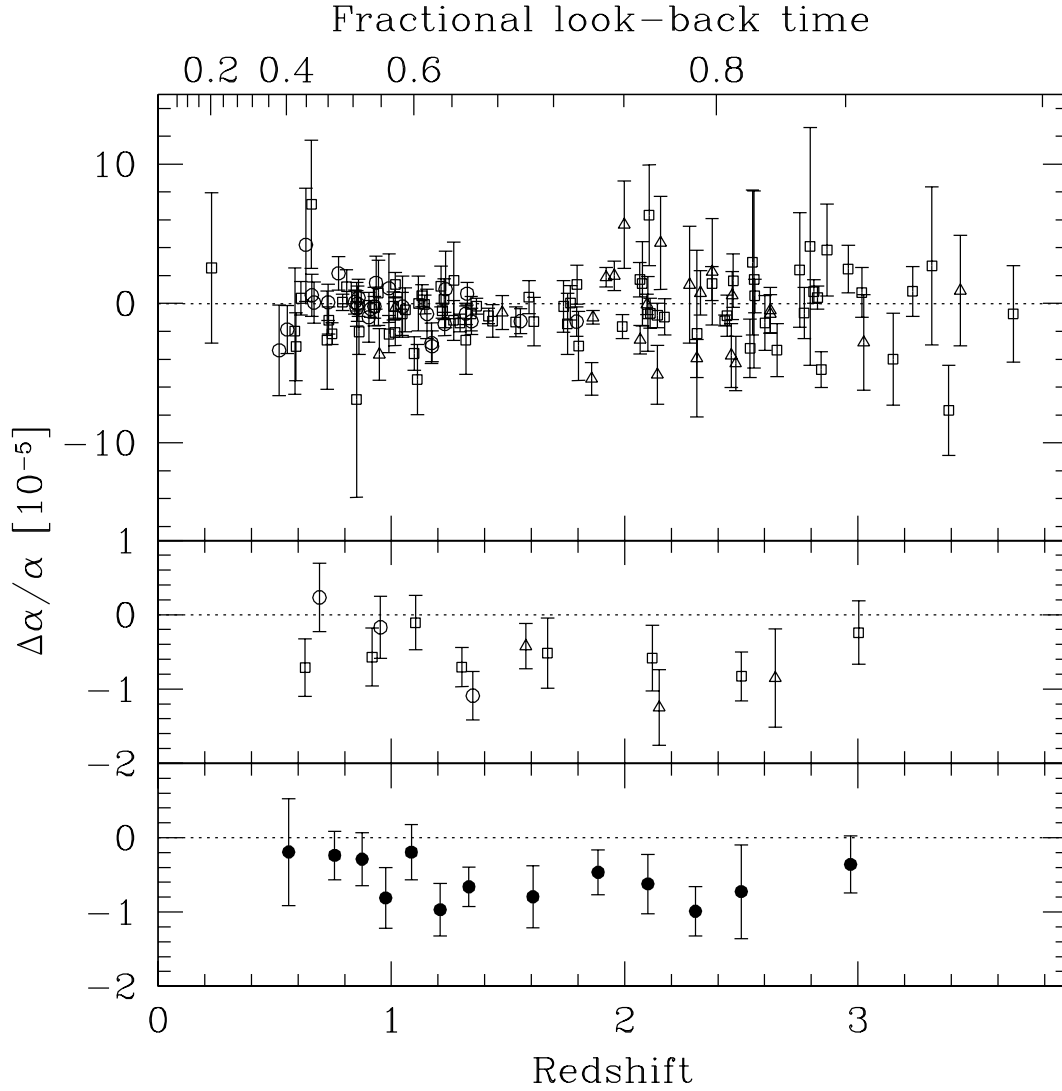


Figure 6. $\Delta\alpha/\alpha$ versus absorption redshift for the previous low- z (open circles), previous high- z (open triangles) and new (open squares) samples. The upper panel shows the raw results and 1σ error bars. The middle panel shows an arbitrary binning of each sample and the lower panel combines all three samples. The redshifts of the binned points are taken as the mean absorption redshift within each bin and the value of $\Delta\alpha/\alpha$ is the weighted mean with its associated 1σ error bar. The upper scale is the look-back time to the absorber as a fraction of the age of the universe ($H_0 = 70 \text{ km s}^{-1} \text{ Mpc}^{-1}$, $\Omega_m = 0.3$, $\Omega_b = 0.04$, $t_0 = 13.47 \text{ Gyr}$).

tal number by the number of bins). We plot the weighted mean for each bin with the associated 1σ error bar. The lower panel combines all three samples. Note the expanded vertical scales on the lower two panels.

4.2 Extra scatter at high- z

In Table 4 we note that the scatter in the total low- z sample is consistent with that expected from the size of the error bars [i.e. $\sigma_{\text{obs}} \approx \sigma_{\text{th}}(\alpha) \approx 1$]. However, at higher z , Fig. 6 shows several values of $\Delta\alpha/\alpha$ which are significantly different from one another, particularly around $z_{\text{abs}} \approx 1.9$. Indeed, Table 4 shows that $\sigma_{\text{obs}} > \sigma_{\text{th}}(\alpha) \approx 1$ and $\chi^2 > 1$ for the total high- z sample and that the previous high- z sample dominates these statistics. Therefore, the weighted mean will not indicate the true significance of α at high- z . Note that the binned points in the lower panels of Fig. 6 will also appear too significant.

There are several reasons why we expect extra scatter at high

z . Consider fitting two transitions, arising from different species, with significantly different line strengths (e.g. Al II $\lambda 1670$ and Ni II $\lambda 1709$ in Fig. 4). Weak components in the high optical depth portions of the strong transition's profile are not necessary to obtain a good fit to the data. Even though the VPFIT χ^2 minimization ensures that constraints on α derive primarily from the optically thin velocity components, these weak components missing from the fit will cause small line shifts. The resulting shift in $\Delta\alpha/\alpha$ is random from component to component and from system to system: the effect of missing components will be to increase the random scatter in the individual $\Delta\alpha/\alpha$ values. We expect this effect to be greater in the high- z sample for several reasons:

- (i) At high z , a larger number of different species are generally available for fitting compared to lower z . The range in optical depths for corresponding velocity components is therefore significantly larger than for the low- z Mg/Fe II systems (compare Figs. 3 and 4), complicating determination of the velocity structure (see

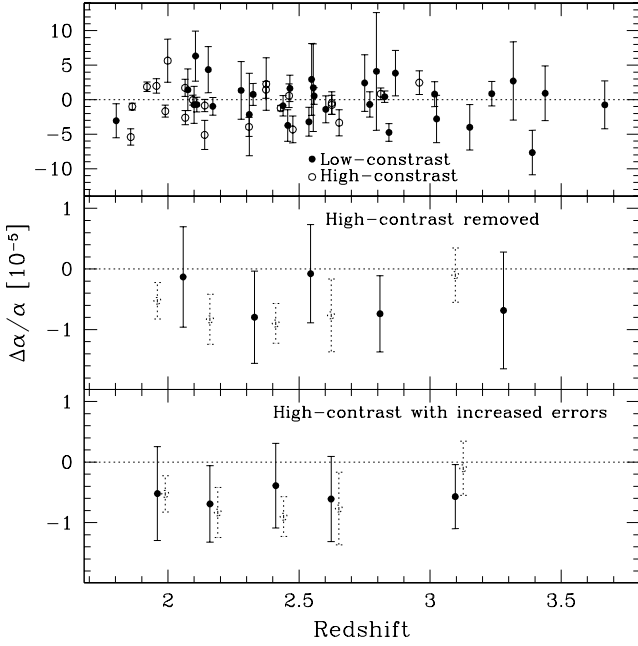


Figure 7. Reducing the extra scatter at high- z . The upper panel identifies the ‘high-contrast’ systems, i.e. where any of the strong Al II, Si II or Fe II transitions *and* any of the weak Cr II, Ni II or Zn II transitions are fitted. These systems are expected to exhibit additional scatter. In the middle panel the high-contrast systems are removed and the binned low-contrast values (solid circles) are compared with the raw values (dotted open circles). In the lower panel the high-contrast error bars have been increased by adding 2.09×10^{-5} in quadrature to the raw errors to match the observed additional scatter. The solid circles are binned values which include the (unaltered) low-contrast systems.

below for details). Abundance and ionization variations will also be more important due to the diversity of species at high- z .

(ii) The high- z sample is dominated by DLAs. If these have a more complex velocity structure, i.e. the number of absorbing components per km s^{-1} is higher than for the Me/Fe II systems, Voigt profile decomposition would be more difficult, increasing the scatter in α .

(iii) In the high- z systems we fit more heavy, i.e. low b_{D} species. Absorption features are therefore closer to the resolution of the instrument, increasing the systematic bias against finding the weaker components.

If these effects cause the extra scatter we observe, the most affected systems will be those with a large range of transition linestrengths. We form such a ‘high-contrast’ sample from the high- z (i.e. $z_{\text{abs}} > 1.8$) sample by selecting those systems in which any of the strong Al II, Si II or Fe II transitions *and* any of the weak Cr II, Ni II or Zn II transitions are fitted. These high-contrast systems are marked with a ‘*’ in Table 3. In the top panel of Fig. 7 these systems (open circles) are delineated from the rest of the high- z sample, i.e. the ‘low-contrast’ systems (solid circles). One immediately notes that the high-contrast sample dominates the extra scatter. The middle panel in Fig. 7 shows the effect of removing the high-contrast systems from the analysis. We give relevant statistics in Table 4: the high-contrast sample comprises 22 systems and, upon removal, χ^2 at high- z drops from 2.179 to 1.207, indicating that the extra scatter is indeed due to the effects mentioned above.

To obtain a more robust estimate of the weighted mean α at high- z , we may increase the individual 1σ errors on α = un-

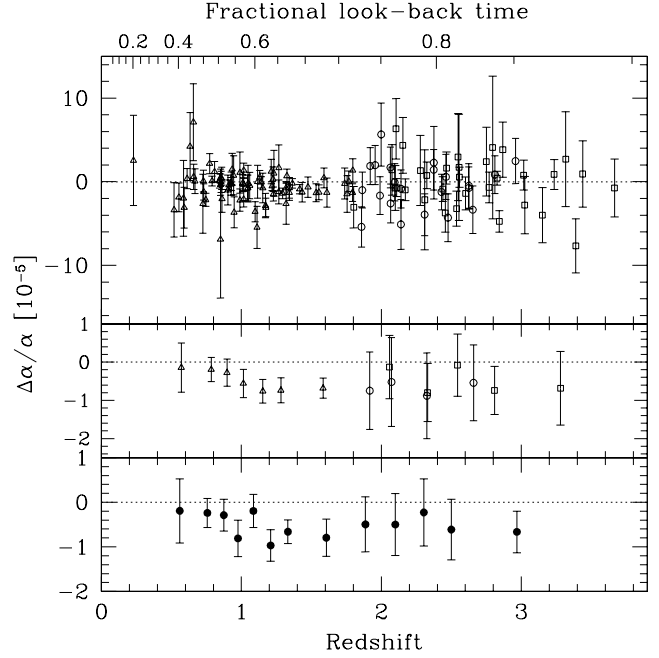


Figure 8. The fiducial sample. The upper panel shows the raw low- z results (solid triangles), the raw values for the low-contrast sample (open squares) and the high-contrast sample with increased error bars (open circles). The middle panel shows a binning of each sample taken separately while the lower panel bins all samples together. The weighted mean for this fiducial sample is $\alpha = (0.543 \pm 0.116) \times 10^{-5}$ and is our most robust estimate of α from the QSO data.

til $\chi^2 = 1$ about the weighted mean for the high-contrast sample. We achieve this by adding 2.09×10^{-5} in quadrature to the error bars of the 22 relevant systems. The resulting binned values of α for the entire high- z sample are plotted in the lower panel of Fig. 7 together with the raw results (shifted for clarity). The statistics in Table 4 indicate that the best estimate of α at high- z is $\alpha = (0.563 \pm 0.291) \times 10^{-5}$. Table 4 also gives the statistics for two other tests: (i) increasing the error bars for all high- z systems until $\chi^2 = 1$ and (ii) removing points which deviate significantly from the weighted mean (i.e. σ -clipping) in the high- z sample until $\chi^2 = 1$. All tests yield similar results.

Throughout the rest of this paper, ‘fiducial sample’ will refer to the raw sample (i.e. the values and 1σ errors in Table 3) but with increased errors on the high-contrast systems at high- z , as described above. We plot the fiducial sample in Fig. 8 for comparison with the raw sample in Fig. 6. Table 4 shows the statistics for the fiducial sample:

$$\alpha = (0.543 \pm 0.116) \times 10^{-5} \quad (9)$$

is our most reliable estimate of the weighted mean α over the redshift range $0.2 < z_{\text{abs}} < 3.7$. This represents 4.7 statistical evidence for a varying α .

4.3 Temporal variations in α ?

In Fig. 9 we overlay the binned fiducial data from Fig. 8 with several fits to the unbinned values of α versus z_{abs} and cosmological time. Note that for the constant α ($d\alpha/dt = 0$) and constant $(d\alpha/dz) = 0$ models we fix α to zero at $z_{\text{abs}} = 0$. The values of χ^2 for the constant α and constant $d\alpha/dz$ fits are

$\chi^2 = 135.22$ and 134.54 respectively. This indicates that a linear increase in α with time,

$$\alpha = (6.40 \pm 1.35) \times 10^{-16} \text{ yr}^{-1}; \quad (10)$$

is preferred over a constant $\alpha = 0$. We estimate the significance of this preference using a bootstrap technique. Each value of α is randomly assigned to one of the measured absorption redshifts and the best fitting constant α is determined. Constructing many such bootstrap samples yields a distribution of χ^2 for the constant α fits. In this procedure we construct low- and high- z bootstrap samples separately since the distribution of α in the real low- and high- z samples may differ (Section 4.2). The χ^2 distribution indicates that 31 per cent of χ^2 values were < 135.22 and 15 per cent were < 134.54 . Thus, the constant $\alpha = 0$ model is preferred over the constant α model only at the 50 per cent confidence level. The latter is preferred over a linear evolution of α with z_{abs} at the 63 per cent level. These confidence intervals are only modestly affected if we analyse the raw sample rather than the fiducial sample. Not distinguishing the low- and high- z samples gives lower confidence levels, i.e. 38 per cent for both cases.

Furthermore, the constant α and $(d\alpha/dz) = 0$ models should be treated with caution. Fixing α to zero (i.e. fixing to the laboratory value) at $z_{\text{abs}} = 0$ may not be valid because of the potential for spatial variations in α . For example, if α varies over

100 Mpc spatial scales and our Galaxy resides in a region with a slightly larger α than the ‘universal mean’, then we should expect to measure a constant negative α rather than an evolution of

α with time. Bekenstein (1979) and Barrow & O’Toole (2001) also note that it is difficult to compare values of α in areas of different gravitational potential without a detailed theory giving both time and space variations of α . If we allow the $z_{\text{abs}} = 0$ value of α to vary, the linear fit against cosmological time is barely altered (see Fig. 9), though somewhat poorly constrained.

4.4 Angular variations in α ?

The fiducial sample can also be used to search for spatial variations in α . If very large scale (> 10 Gpc) spatial variations exist, one might expect α to be different in different directions on the sky. For the fiducial sample, we plot the distribution of α over Galactic coordinates (l, b) in Fig. 10. All redshift information is removed by taking all absorption systems along a single QSO sight-line and collapsing them to a single weighted mean value of α . We also combine independent values from the same QSO in different observational samples (see Section 4.7). The grey-scale indicates the weighted mean α and the size of each point scales with the significance with respect to the overall weighted mean of the fiducial sample, $S_{0.543}$ (equation 9).

We used a χ^2 minimization algorithm to find the best-fit dipole in the angular distribution of α . We first constructed a grid of directions in equatorial coordinates, (RA, DEC). For each direction, a cosine fit to α as a function of the angular distance, θ , to each absorption system, yields an amplitude for the dipole, $(\alpha)_{\text{d}}$, defined by

$$\alpha(\theta) = \frac{D}{w} + \frac{E}{d} \cos \theta; \quad (11)$$

Fig. 11 shows the best-fit dipole which has an amplitude $(\alpha)_{\text{d}} = (0.43 \pm 0.25) \times 10^{-5}$. The pole is in the direction P (RA, DEC) = (50 hr, 48°) or P (l, b) = (340°, 39°) as marked on Fig. 10. We also mark the anti-pole,

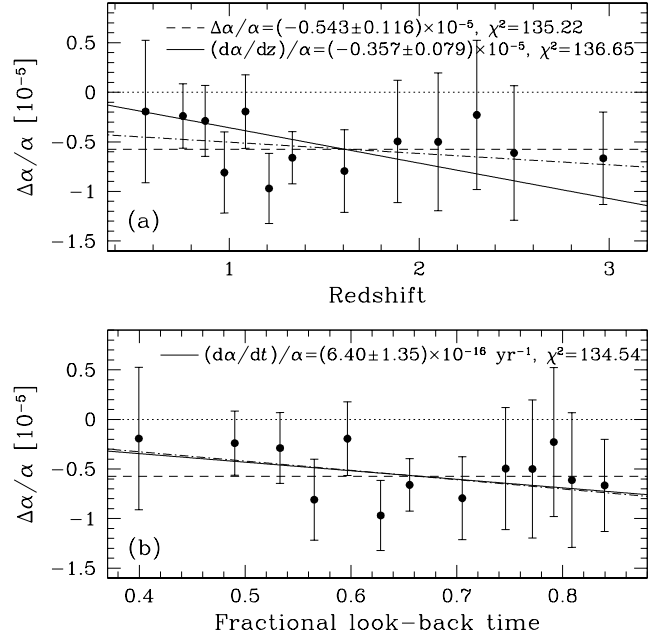


Figure 9. Temporal variation in α . (a) The points are the binned values of α for the fiducial sample plotted versus redshift. The dashed line is the weighted mean and the solid line is a fit to the unbinned data fixed to $\alpha = 0$ at $z_{\text{abs}} = 0$. The dot-dashed line is a fit with the $z_{\text{abs}} = 0$ value allowed to vary. The values of χ^2 indicate that the constant $\alpha = 0$ model is preferred. (b) Same as (a) but versus fractional look-back time. The values of χ^2 indicate that a linear increase in α with time is preferred.

α , and the cosmic microwave background (CMB) pole and anti-pole directions (P_{CMB} and A_{CMB} , Lineweaver et al. 1996) for comparison.

The limited range of angular separations in Fig. 11 severely limits the dipole interpretation. Although the dipole amplitude is significant at the 1.7 σ level, a bootstrap analysis similar to that in the previous section indicates that the dipole model is not significantly preferred over the constant $\alpha = 0$ (i.e. monopole) model. Bootstrap samples were formed by randomizing the values of α over the QSO sight-line directions. Again, we treated the low- and high- z samples separately, combining them only to find the best-fit dipole directions. The resulting probability distribution for $(\alpha)_{\text{d}}$ indicates that values at $> 1.7 \sigma$ significance occur 40 per cent of the time by chance alone. Analysing the raw sample gives a similar confidence level. Therefore, the data do not support significant angular variations in α . There is also no evidence for angular variations in the low- z and high- z samples taken separately.

4.5 Spatial correlations in α ?

If spatial variations in α do exist at the $\alpha = 10^{-5}$ level then one expects to see additional scatter in the raw values of α in Fig. 6. However, as noted previously, the statistics in Table 4 indicate that the scatter at low z is consistent with the size of the error bars and so we have no evidence for spatial variations in α for $z_{\text{abs}} < 1.8$. The additional scatter at higher z may provide evidence for spatial variations but this seems unlikely given the discussion in Section 4.2.

We performed a more thorough search for spatial variations by calculating the two-point correlation function for α . Consider

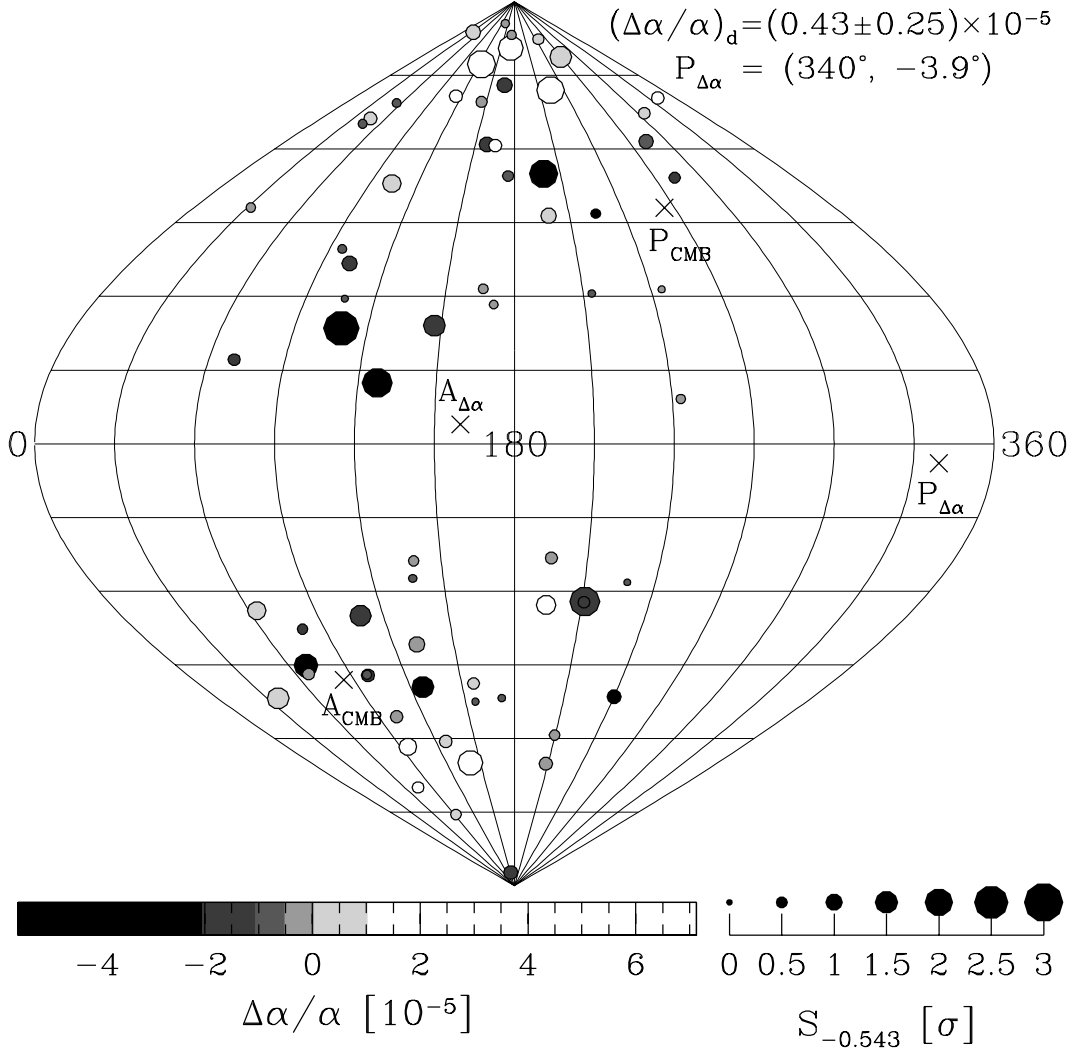


Figure 10. The distribution of $\Delta\alpha/\alpha$ in Galactic coordinates (l, b). All fiducial values along a single QSO sight-line (i.e. for many absorption clouds and/or repeated, independent QSO observations) are collapsed to a single weighted mean. The value of $\Delta\alpha/\alpha$ is given by the grey-scale and the size of each point scales with the significance, $S_{-0.543}$, of the departure from the overall weighted mean of the fiducial sample (equation 9). The best-fit dipole has an amplitude $(\Delta\alpha/\alpha)_d = (0.43 \pm 0.25) \times 10^{-5}$ with its pole and anti-pole in the directions P and A . However, a bootstrap analysis indicates that the dipole model is preferred over the constant $\Delta\alpha/\alpha$ model at only the 60 per cent confidence level. We plot the CMB pole and anti-pole for comparison. (The on-line version of this figure is colour-coded and is also available from <http://www.ast.cam.ac.uk/~mim/pub.html>)

two absorption systems with fiducial values of $\Delta\alpha/\alpha_1$ and $\Delta\alpha/\alpha_2$. The two-point correlation function, C_{12} , is then

$$C_{12} = \frac{(\Delta\alpha/\alpha_1 - \bar{\Delta\alpha/\alpha})(\Delta\alpha/\alpha_2 - \bar{\Delta\alpha/\alpha})}{\sigma^2}; \quad (12)$$

where $\bar{\Delta\alpha/\alpha}$ is the mean value of $\Delta\alpha/\alpha$ over the entire sample.

In Fig. 12 we plot the correlation function versus the comoving separation between the absorption systems (e.g. Liske 2003). We used a Monte Carlo technique to estimate the mean two-point correlation function, $C(\Delta r)$, and 68 per cent confidence interval for each bin. Synthetic values of $\Delta\alpha/\alpha$ were drawn randomly from Gaussian distributions centred on the measured values with 1 σ widths equal to the fiducial 1 σ errors. Where independent observations of an absorption system exist (Section 4.7), we centred the Gaussian on the weighted mean value and used the 1 σ error in the weighted mean. For each bin, the mean $C(\Delta r)$ was found from all pairs of absorption systems with comoving separations within the bin. In Fig. 12 we plot the mean and rms of this quantity, rep-

resented by a point and error bar. Fig. 12 shows no evidence for significant spatial correlations in $\Delta\alpha/\alpha$ over 0.2–13 Gpc (comoving) scales.

4.6 Comparison with previous analysis

The majority of velocity structures fitted to the previous samples are unchanged from M01a. For the low- z sample, the raw values of $\Delta\alpha/\alpha$ are similar to those found in M01a, as shown in Fig. 13. In M01a, the weighted mean was $\Delta\alpha/\alpha = (-0.70 \pm 0.23) \times 10^{-5}$ for this sample. The primary reason for the slightly less negative value of $\Delta\alpha/\alpha$ we find here [from Table 4, $\Delta\alpha/\alpha = (-0.51 \pm 0.22) \times 10^{-5}$] is the increased q coefficients for the low- z Fe II transitions (i.e. those with $\lambda_0 > 2000\text{\AA}$ in Table 2). For the previous high- z sample, Fig. 13 shows that the raw values of $\Delta\alpha/\alpha$ found here are, in individual cases, somewhat different to those found in M01a. This is primarily due to the large change in the Fe II 1608 q coefficient (see Section 2.2). However, since the high- z sample is charac-

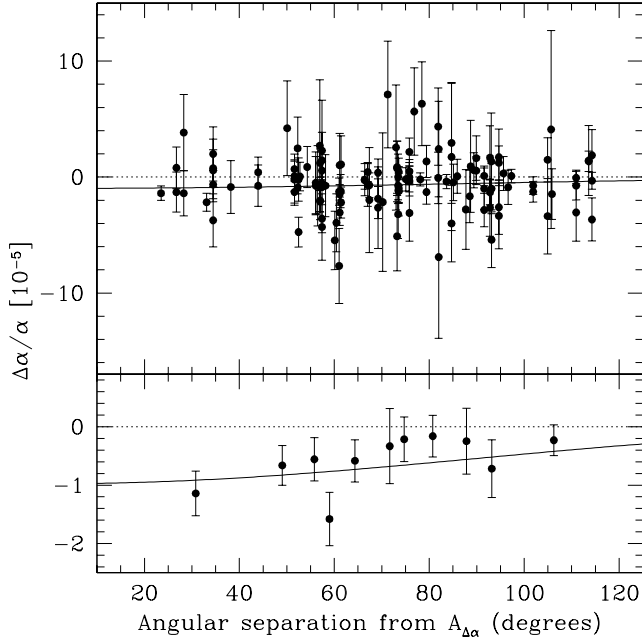


Figure 11. Best-fit dipole to the angular distribution of $\xi = \xi_{\text{dipole}}$ in Fig. 10. The pole lies in the direction $\hat{p} = (\ell, b) = (340^\circ; 3.9^\circ)$. The upper panel shows the distribution of ξ with angular separation from the anti-pole, $A_{\Delta\alpha}$. The lower panel shows a binning of the results. The solid line is the best-fit cosine with an amplitude $(\xi/\alpha)_{\text{dipole}} = (0.43 \pm 0.25) \times 10^{-5}$. However, the limited angular coverage of QSO sight-lines clearly undermines confidence in this dipole interpretation.

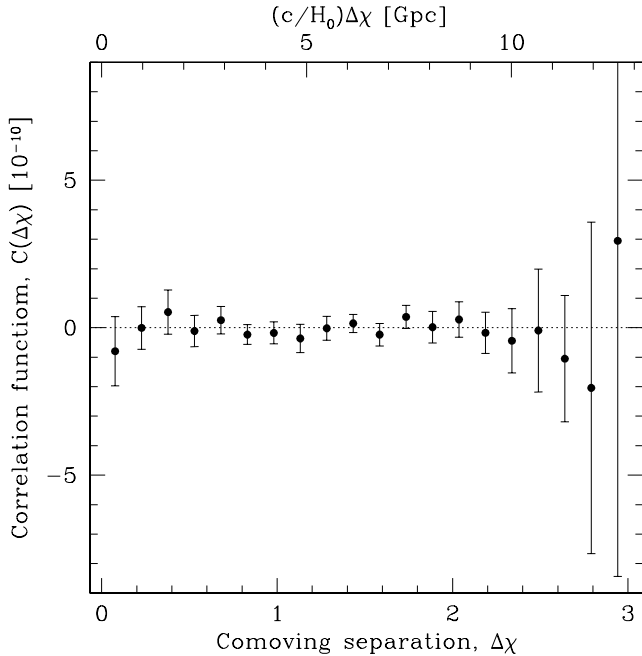


Figure 12. The two-point correlation function for ξ , $C(\xi)$, as a function of comoving separation between absorption clouds, $\Delta\chi$ ($H_0 = 70 \text{ km s}^{-1} \text{ Mpc}^{-1}$, $\xi_{\text{min}} = 0.3$, $\xi_{\text{max}} = 0.7$). The values and errors were obtained with a Monte Carlo technique. However, since each value of ξ may contribute to many bins, the bins are not independent.

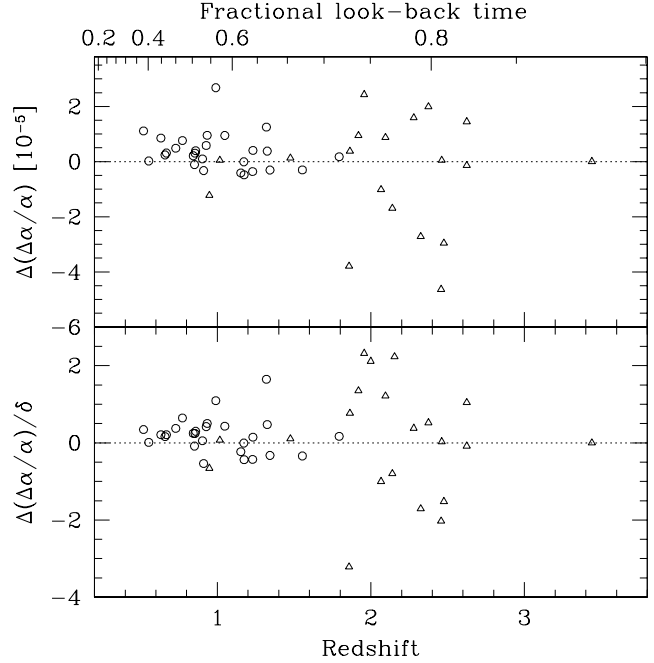


Figure 13. Comparison with previous analysis in M01a. The upper panel compares the raw values of $\xi = \xi_{\text{dipole}}$ found here with those in M01a [$\xi = \xi_{\text{dipole}} = (\xi/\alpha)_{\text{M01a}}$] for the previous low- z (open circles) and previous high- z (open triangles) samples. The lower panel shows a measure of the significance of this difference: (ξ/α) normalized by the 1σ error in Table 3. For the low- z data we find a slightly more positive ξ on average because the q -coefficients for the $\lambda_0 > 2000\text{\AA}$ Fe II transitions have been revised to slightly higher values. The larger scatter seen in (ξ/α) for the high- z systems is due mainly to the large change in the Fe II 1608\AA q coefficient (see Section 2.2).

terized by many different transitions with a diverse range of q coefficients, the overall weighted mean ξ found in M01a compares well with the value found here: $\xi = (0.67 \pm 0.33) \times 10^{-5}$ and $(0.67 \pm 0.24) \times 10^{-5}$ respectively.

4.7 Repeated observations

Several QSOs in our sample have been observed independently by two different groups: the new sample contains 7 absorption systems which are also (independently) contained in the previous samples and two independent spectra of the $z_{\text{abs}} = 2.6253$ system towards GB 1759+7539 are contained in the previous high- z sample. We compare the values of ξ from the raw sample for these repeated systems in Fig. 14. The lower panel may indicate some evidence for systematic errors in individual points (i.e. some additional scatter may exist). However, the value of χ^2 with respect to zero difference is $\chi^2 = 13.33$ which, for 7 degrees of freedom, has a 6.4 per cent probability of being exceeded by chance. Evidence for additional scatter is therefore rather marginal.

5 SYSTEMATIC EFFECTS

The above results represent strong statistical evidence for a smaller ξ in the QSO absorption clouds. The fact that three different samples show the same effect leaves little doubt that we do detect small line shifts in the data. The central question is now whether these line shifts are due to systematic errors or really due to varying ξ .

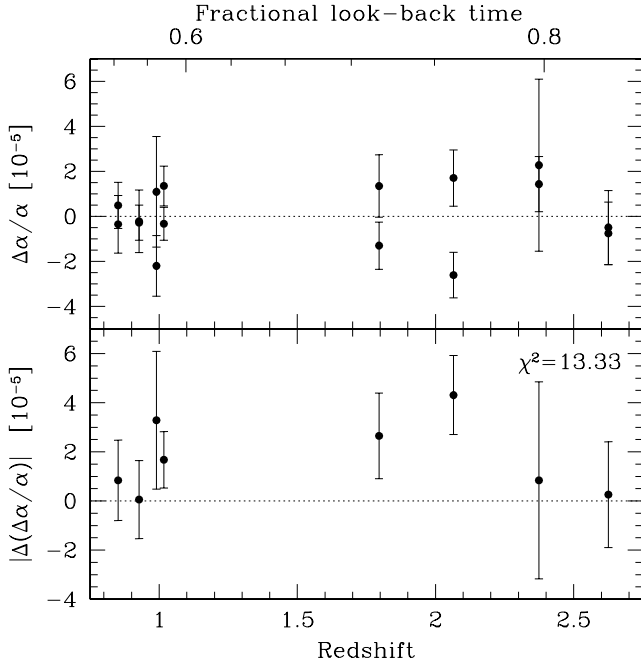


Figure 14. Repeated absorption systems. The upper panel shows the raw values of $\Delta\alpha/\alpha$ for those systems which have been observed independently by different groups. The absolute difference is shown in the lower panel. For 7 degrees of freedom, the indicated value of χ^2 will be exceeded 6.4 per cent of the time by chance alone, providing only marginal evidence for significant additional random errors.

In M01b we considered potential systematic effects due to laboratory wavelength errors, wavelength miscalibration, atmospheric dispersion effects, unidentified blending transitions, isotopic and/or hyperfine structure effects, intrinsic instrumental profile variations, spectrograph temperature variations, heliocentric velocity corrections, kinematic effects and large scale magnetic fields. Below we extend this initial search to include the entire Keck/HIRES sample.

5.1 Kinematic effects

In order to measure $\Delta\alpha/\alpha$ with the MM method one must assume that corresponding velocity components of different ionic species have the same redshift. Velocity segregation could arise through chemical abundance gradients combined with differential velocity fields. These effects may also generate departures from Voigt profiles. The low- z Mg/Fe II systems would be more sensitive to any velocity segregation between species due to the simple arrangement of q coefficients (see Fig. 1). For the high- z systems, the effect on $\Delta\alpha/\alpha$ for an individual system would be minimized due to the diversity and complicated arrangement of q coefficients.

Inhomogeneous photoionization throughout the absorption complex is also a possibility. With the exception of Mg I and Al III, the species in our analysis are singly ionized, have very similar ionization potentials, IP^+ , all above the Lyman limit and the corresponding neutral ions have similar ionization potentials, IP^0 , all below the Lyman limit (see Table 2). Thus, the absorption from different ionic species, associated with a given velocity component, should arise co-spatially. However, variations in the incident radiation field could cause weak components in the singly ionized species to appear very strong in Mg I or Al III. Spurious shifts in $\Delta\alpha/\alpha$ could be introduced if a strong Mg I or Al III component

was mistakenly tied to a nearby ($\Delta v \approx 0.5 \text{ km s}^{-1}$) singly ionized component⁷.

However, as we pointed out in M01b, these kinematic shifts in $\Delta\alpha/\alpha$ are themselves random over a large ensemble of random sight-lines. If kinematic effects are significant, they act only to increase the scatter in the values of $\Delta\alpha/\alpha$ beyond what is expected on the basis of the statistical errors alone. The value of χ^2 for the low- z sample in Table 4 is 1 and so the low- z data present no evidence for significant kinematic effects. One may interpret the extra scatter in $\Delta\alpha/\alpha$ observed at high- z as evidence for such effects, though we discuss other, more likely, mechanisms for producing this scatter in Section 4.2.

Despite the random nature of kinematic effects over a large number of velocity components and absorption systems, we discuss below the contributory factors to potential effects on small velocity scales for individual velocity components.

5.1.1 Small-scale velocity structure and equilibrium in QSO absorbers

Detailed kinematic studies of QSO absorbers indicate that a disk+halo model provides a reasonable description of the absorption systems (Briggs et al. 1985; Lanzetta & Bowen 1992; Wolfe & Prochaska 2000b; Churchill & Vogt 2001). Alternative models exist, including multiple merging clumps bound to dark matter halos (Haehnelt, Steinmetz & Rauch 1998; McDonald & Miralda-Escudé 1999; Maller et al. 1999) and outflows from supernovae winds (Nulsen, Barcons & Fabian 1998; Schaye 2001). For disk+halo models of Mg/Fe II systems, the disk component is strongly saturated and spread over small velocity scales whereas the halo component is broadly spread in velocity space and causes the lower column density absorption. The constraints on $\Delta\alpha/\alpha$ in the Mg/Fe II systems are therefore dominated by velocity components arising in the outer parts of galaxy halos. The constraints on $\Delta\alpha/\alpha$ from DLAs arise either from low abundance, hence unsaturated, species (e.g. Ni II, Cr II, Zn II), or from optically thin components flanking the saturated ones (e.g. Fe II 1608 or Al II 1670).

However, the *large-scale properties of the absorbing gas have no influence on estimates of $\Delta\alpha/\alpha$* . Galactic rotation or large-scale galactic winds are unimportant. The empirical fact that we find excellent agreement between the redshifts of individual velocity components down to $\sim 0.3 \text{ km s}^{-1}$ illustrates this. Any contribution to the scatter in $\Delta\alpha/\alpha$ comes only from the detailed properties of gas on velocity scales typical of the observed b parameters, i.e. $\sim 5 \text{ km s}^{-1}$.

Given the importance of small-scale properties in the determination of $\Delta\alpha/\alpha$, it is relevant to ask whether the gas is in dynamic equilibrium on these scales. For the low- z Mg/Fe II systems, a recent detailed study (Churchill, in preparation) suggests that the column density ratio $N(\text{Mg II})/N(\text{Fe II})$ appears not to change systematically across an absorption complex. A similar chemical uniformity is found for the majority of high- z systems (Prochaska 2003). This implies that, if not in equilibrium, the gas is well mixed, i.e. absorption lines of different species arise co-spatially.

⁷ We find no additional scatter in $\Delta\alpha/\alpha$ for systems containing Mg I or Al III and so have no evidence for such effects. We discussed the specific case of Al III in M01b, finding that its velocity structure followed very closely that of the singly ionized species. See also discussion in Wolfe & Prochaska (2000a)

Photoionization models also suggest gas in photoionization equilibrium with an ambient extra-galactic UV background. If this is correct, local equilibrium may be valid. Any redshift evolution of the number of absorption lines per unit redshift interval, over and above that expected due to cosmology alone, could be explained by cosmological evolution of the integrated background UV flux (e.g. Rao & Turnshek 2000).

Thus, there is evidence to suggest that no gross changes in physical conditions occur over large velocity scales across an absorption complex. This may imply that we should not expect to find abundance variations and non-equilibrium on small scales. If this is incorrect, one expects departures from a Maxwellian velocity distribution in the absorbers, the assumption of which is inherent in fitting Voigt profiles. We note in passing that no evidence currently exists for non-Voigt profiles (e.g. Outram et al. 1999), despite expectations from hydrodynamic simulations of large-scale structure formation (Outram et al. 2000).

5.1.2 Comparison with the ISM

In contrast to the previous section, analogy with the interstellar medium (ISM) in our own Galaxy suggests that non-equilibrium could apply on very small scales. Andrews, Meyer & Lauroesch (2001) used stars in a background globular cluster, M92, to probe the kinematics on scales defined by the separation between the lines of sight at the absorber. They find significant variations in Na I column densities in the ISM on scales as small as 1600 AU (or 0.01 pc). Even smaller-scale details come from measurements of temporal variation of Na I and K I absorption lines, implying non-equilibrium scales ~ 10 – 100 AU (Crawford et al. 2000; Lauroesch, Meyer & Blades 2000; Price, Crawford & Barlow 2000). Although these ISM cloud sizes are small compared to estimates for individual QSO absorption cloud components, ~ 10 – 100 pc (Churchill & Vogt 2001), the characteristic size for a QSO continuum emission region may be $\sim 10^3$ pc. The lines of sight to opposite edges of the QSO therefore probe similar size scales as the Galactic ISM studies. However, it should be noted that the gas densities are very different and so the comparison should be treated with caution.

The ISM analogy may also allow us to estimate an upper limit on the velocity segregation in QSO absorption clouds. Some theories argue that gravity may be important for cloud confinement on small size scales in the Galactic ISM (e.g. Walker & Wardle 1998). If gravity plays a significant role in QSO absorption systems on similar scales, we could apply a simple stability condition on the velocity dispersion, $v^2 = GM/R$, where M and R are the cloud mass and radius. Estimates for individual cloud sizes vary but adopting $R = 10$ pc and $M = 30 M_\odot$ (Churchill & Vogt 2001) we find $v \lesssim 0.1$ km s $^{-1}$. This provides an upper limit on the velocity shift between different species. For one single Mg/Fe II velocity component, this translates into an error on an individual α measurement of roughly $\delta\alpha = \delta v / c \approx 0.3 \times 10^{-5}$. However, this would be randomized over ~ 100 observations (and over many velocity components), producing a maximum overall effect which is 20 times smaller than that observed.

5.2 Line blending

We distinguished between *random* and *systematic* line blending in M01b. We discuss both cases and their effect on α below.

5.2.1 Random blends

Random blends can occur when many absorption clouds lie along the line of sight to the QSO, including any interstellar material and the Earth's atmosphere. In general, random blends can only have a random effect on α and so can not have caused the systematically non-zero values observed. Two distinct categories of random blend can be identified:

(i) Strong blends. Lyman- γ forest absorption lines would cause numerous strong blends. However, if MM transitions fell into the Lyman- γ forest region, we generally did not fit them. If the velocity structure of one of our MM transitions is obviously affected by a random blend then we modify our fit for that transition according to the identity of the interloper. If the interloper is a MM transition (i.e. one with a precise laboratory wavelength listed in Table 2), and its velocity structure can be constrained using other associated MM transitions at the interloper's redshift, then we include the interloper in the fit. In general, the laboratory wavelengths of non-MM transitions (e.g. C IV $\lambda 1548$ and 1550) are not known to high precision. Therefore, if the interloper and/or the associated transitions are not MM transitions, possible errors in the laboratory wavelengths could have a significant effect on α . In these cases, and if the velocity structure of the interloper was both simple and clear, we freed its redshift parameters, not tying it to any associated transitions. In all other cases, we either masked the blended data out of the fit or simply rejected that MM transition altogether.

(ii) Weak blends. It is possible that weak, random interlopers exist in our data but were not identified in our analysis. For example, numerous broad ($\text{FWHM} = 20$ – 2000 km s $^{-1}$), weak (equivalent width < 0.1 Å), diffuse interstellar absorption bands have been discovered in stellar spectra (e.g. Herbig 1975; Jenniskens & Desert 1994). The narrower of these lines may blend with some velocity components of individual MM transitions, causing slight, apparent line shifts. However, since our absorption systems lie at a range of redshifts and since many different transitions are fitted to arrive at a final value of α , it is unlikely that such weak interlopers have significantly affected our results.

5.2.2 Systematic blends

A systematic blend occurs when two ionic species are in the same absorption cloud and have transitions with similar rest wavelengths. Such a blend could mimic a systematic shift in α . We have explored two approaches to this problem:

(i) In M01b we attempted to identify candidate blends by searching atomic line databases for transitions lying close to the laboratory wavelengths of the MM transitions. Simulations of various blends indicated that, in order to cause a significant and systematic shift in α , the interloping transition must lie within ~ 10 km s $^{-1}$ of the 'host' line. No possible blending transitions satisfying this criterion could be found in Moore (1971) or the Vienna Atomic Line Database⁸ (VALD, Piskunov et al. 1995; Kupka et al. 1999).

We have now extended our search criterion to include potential interlopers lying up to 100 km s $^{-1}$ away from the host MM transitions. We have identified two possible interlopers lying to the red of the Zn II $\lambda 2026$ transition:

⁸ Available at <http://www.astro.univie.ac.at/vald>

(a) Cr II 2026.269 ($v = 19 \text{ km s}^{-1}$) has an oscillator strength $f = 0.0047$ (VALD; correcting a typographical error in M01b). Using the largest value of $N(\text{Cr II})/N(\text{Zn II})$ from our data, simulations of this blend suggest a negligible effect on λ_{ThAr} (see M01b for details).

(b) Mg I 2026.477 ($v = 50 \text{ km s}^{-1}$) has an oscillator strength $f = 0.1154$ (Morton 1991) and was apparent in six of the high- z systems. However, in four cases the velocity structure is narrow enough that the Mg I interloper does not overlap and blend with the Zn II line. In the remaining two cases we fitted the Mg I interloper and left the redshift parameters free (i.e. we did not tie the Mg I velocity structure to that of the other MM transitions). This has the effect of removing any constraints the blended Zn II components may have on λ_{ThAr} . We checked the resulting values of λ_{ThAr} against those found after completely masking out the blended portion of the Zn II velocity structure, finding them to be consistent. Also, completely removing the Zn II 2026 transition from the analysis of these systems produced very little change in λ_{ThAr} .

Note that the atomic line databases searched are not complete and that we have not considered molecular interlopers. We therefore compliment the treatment above with the following test.

(ii) To assess the significance of any unknown blends, we may separately remove most transitions from the analysis and re-fit to find a new value of λ_{ThAr} . If the new and old values of λ_{ThAr} are significantly different then one interpretation is that the transition removed is affected by an unknown systematic blend. In M01b we found no evidence for blends in this way. We update this line-removal analysis in Section 5.7.1 and reach the same conclusion.

In summary, we find that neither random or systematic line blending has significantly affected the values of λ_{ThAr} .

5.3 Wavelength miscalibration

The QSO CCD images are wavelength calibrated by comparison with ThAr emission lamp spectra which are generally taken both before and after each QSO exposure. A polynomial wavelength solution is obtained by centroiding a standard set of ThAr lines which are strong and (appear to be) unblended in the particular ThAr lamp in use. If one or more of the ThAr lines in this standard set are misidentified or, in a more subtle way, lead to long range miscalibrations of the wavelength scale, then a systematically non-zero λ_{ThAr} would be found. This effect would be particularly problematic in the low- z absorption systems where all values of λ_{ThAr} would be affected in the same way by such a low-order distortion of the wavelength scale (see Fig. 1).

5.3.1 The ThAr calibration test

The effect of any ThAr miscalibrations on the values of λ_{ThAr} can be estimated directly using a technique proposed and demonstrated in M01b: we analyse sets of ThAr emission lines in the same way we analyse sets of QSO absorption lines. If no calibration error exists then one should obtain $\lambda_{\text{ThAr}} = 0$ for each absorption system.

We provide a detailed description of this ThAr test in M01b, the main steps being as follows. First we select several independent sets of ThAr emission lines from sections of spectra which correspond to the observed wavelengths of the QSO absorption lines. Each set of lines therefore corresponds to, and has been selected in

an analogous way to, one QSO absorption system. Selecting several (typically 3–7) different sets of ThAr lines allows a more robust estimate of λ_{ThAr} for each absorption system and provides a cross-check on its 1σ uncertainty.

We fit Gaussian profiles to the emission lines with the same modified version of VPFIT used to fit Voigt profiles to the QSO absorption lines. In order to relate any measured ThAr line shifts directly to a value of λ_{ThAr} , we assign to each ThAr line the q coefficient corresponding to the QSO absorption line falling in that part of the spectrum. That is, we treat the ThAr lines as if they were QSO absorption lines and derive a value of λ_{ThAr} using the MM method.

5.3.2 Results and discussion

ThAr spectra were readily available for 118 of the 128 absorption systems in our total sample. We applied the above ThAr test to these spectra and obtain the results presented in Fig. 15. Comparing the QSO results (raw sample) in panel (a) with the ThAr results in panel (b) we immediately see that miscalibrations of the wavelength scale did not systematically affect the overall value of λ_{ThAr} . This is particularly emphasized in panel (e) which compares binned raw values of λ_{ThAr} and λ_{ThAr} . We tabulate various statistics for the ThAr test in Table 4 for direct comparison with the QSO results. Notably, the overall weighted mean value, $\lambda_{\text{ThAr}} = (0.4 \pm 0.8) \times 10^7$, is two orders of magnitude below the observed value of $\lambda_{\text{ThAr}} = 0$.

Panel (c) of Fig. 15 shows an expanded view of the ThAr results which clearly demonstrate a similar ‘extra scatter’ to the high- z QSO sample (see Section 4.2). The extra scatter has a similar origin as for the high- z QSO results: close inspection of any portion of ThAr spectrum reveals a plethora of weak emission lines and so the fit to any given strong ThAr emission line will be affected by weak blends. The ThAr lines are of such high S/N that significant extra scatter ensues. This effect would produce uncorrelated deviations in λ_{ThAr} from point to point, as observed. Another interpretation may be that the extra scatter presents evidence for ThAr line misidentifications. However, if these were important, one would expect a correlation between λ_{ThAr} and λ_{ThAr} . We observe no such correlation.

The ThAr results in Fig. 15 also illuminate discussion of potential instrumental profile (IP) variations and their effect on λ_{ThAr} . Valenti, Butler & Marcy (1995) have derived the HIRES IP for several positions along a single echelle order, finding that the IP is slightly asymmetric and that this asymmetry varies slightly along the order. However, to a first approximation, the ThAr and QSO light paths through the spectrograph are the same. The ThAr results in Fig. 15 therefore strongly suggest that IP asymmetries (and variations thereof) do not contribute significantly or systematically to λ_{ThAr} . One possibility is that the ThAr and QSO light follow very different and possibly wavelength dependent paths through the spectrograph to the CCD. We explore this possibility in Section 5.6 in the context of atmospheric dispersion effects.

We conclude this section by emphasizing the reliability of the wavelength scale as derived from the ThAr spectra: we directly measure the effect of any ThAr miscalibrations on λ_{ThAr} and find it to be negligible. One objection to the reliability of the MM method has been that fitting transitions which fall on different echelle orders may lead to systematic errors (Varshalovich et al. 2000; Ivanchik et al. 2002). The ThAr test in Fig. 15 (and figure 2 in M01b) clearly demonstrates that these concerns are unfounded.

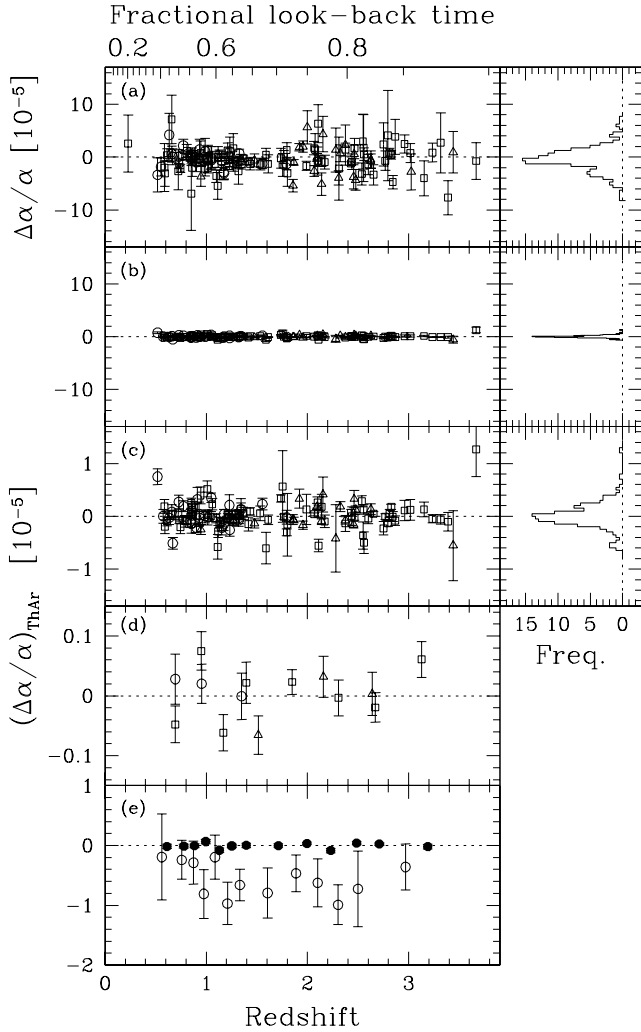


Figure 15. Comparison between the raw QSO results [panel (a)] and the ThAr calibration error [panel (b)] for the previous low- z (open circles), previous high- z (open triangles) and new (open squares) samples. The $(\Delta\alpha/\alpha)_{\text{ThAr}}$ scale is expanded by a factor of 10 in panel (c). Panel (d) shows binned values for the three sub-samples and panel (e) compares the binned values for the total ThAr (solid circles) and raw QSO (open circles) samples. The weighted mean of the ThAr results is $(\Delta\alpha/\alpha)_{\text{ThAr}} = (0.4 \pm 0.8) \times 10^{-7}$.

5.4 Spectrograph temperature variations

The refractive index of air within the spectrograph depends on temperature (and also on pressure, but this is a smaller effect). If the temperature during the QSO exposure, T_{QSO} , is 15 K higher than that during the ThAr calibration exposure, T_{ThAr} , the wavelength scale applied to the QSO frame would be distorted, resulting in $\epsilon = +1 \times 10^{-5}$ for a typical Mg/Fe II system (see M01b for details). Note that a systematically non-zero ϵ can only be introduced for the Mg/Fe II systems if T_{QSO} is systematically higher or lower than T_{ThAr} .

Such an effect can be minimized if the ThAr calibration exposures are taken immediately before and/or after the QSO exposures or if the spectrograph is temperature stabilized (e.g. VLT/UVES). The former was generally the case for our observations. We have used image header information to calculate $T = \text{HT}_{\text{QSO}} / \text{HT}_{\text{ThAr}}$ for each QSO in each sample, where the average is taken over all QSO and ThAr exposures. We find mean values of $T =$

Table 5. The percentage terrestrial isotopic abundances of the atoms used in our analysis (Rosman & Taylor 1998). The second column shows the mass number, A , of the isotope with the highest abundance and ΔA is defined relative to this (negative values representing lighter isotopes).

Atom	A	2	0	+1	+2	+3	+4	+6
Mg	24		79.0	10.0	11.0			
Al	27		100.0					
Si	28		92.229	4.683	3.087			
Cr	52	4.3	83.8	9.5	2.4			
Fe	56	5.8	91.8	2.1	0.3			
Ni	58		68.08		26.22	1.14	3.63	0.93
Zn	64		49		28	4	19	1

0.04 ± 0.02 K and $T = 0.2 \pm 0.1$ K for the previous low- and high- z samples, and $T = 0.013 \pm 0.006$ K for the new sample. It is therefore clear that our values of ϵ are not affected by spectrograph temperature variations.

5.5 Isotopic and hyperfine structure effects

As stated in Section 2.2, the only species for which full isotopic and hyperfine structures are known are Mg I, Mg II and Al III. We obtained an estimate of the Si II isotopic structures by scaling the Mg II 2796 structure by the mass shift, equation 7. In this section we investigate systematic errors that could result from ignorance of the isotopic/hyperfine structures for other species and from any evolution of the isotopic ratios and/or hyperfine level populations.

5.5.1 Differential isotopic saturation

For the transitions of Cr II, Fe II, Ni II and Zn II, the laboratory wavelengths in Table 2 are *composite* values only. The composite wavelengths are only strictly applicable in the optically thin regime (linear part of the curve of growth). Consider an absorption line with several isotopes. As the dominant (highest abundance) isotope saturates, the weaker isotopes will have increased influence on the fitted line centroid. This could lead to systematic errors in ϵ .

Table 5 shows the terrestrial isotopic abundances for the atoms used in the MM method. Note that the abundance is quite distributed and asymmetric for Ni, Zn and, to a lesser extent, Cr. If the isotopic components of the transitions of these species were widely spaced in wavelength then differential isotopic saturation may be an important effect. However, the Cr, Ni and Zn lines are always weak in our QSO spectra, typically absorbing only 20 per cent of the continuum. Using only the composite wavelengths for transitions of these species is therefore justified.

Although the Fe abundance is strongly centred on the ^{56}Fe isotope, the Fe II transitions in our QSO spectra are often saturated. The possible effect of differential isotopic saturation for Fe should therefore be tested. The mass isotopic shift (equation 7) for Fe transitions should be ~ 5 times smaller than for those of Mg. Therefore, using only composite wavelengths of Mg and Si transitions in our analysis (instead of the full isotopic structures) should place a firm upper limit on the possible effect from Fe II.

We have conducted such a test with our total sample: we use composite wavelengths for the Mg I, Mg II and Si II isotopic structures and refit our spectra to find values of $(\Delta\alpha/\alpha)_{\text{comp}}$. We also use composite wavelengths for the Al III hyperfine structures (see Section 5.5.2). We provide a detailed discussion of the expected

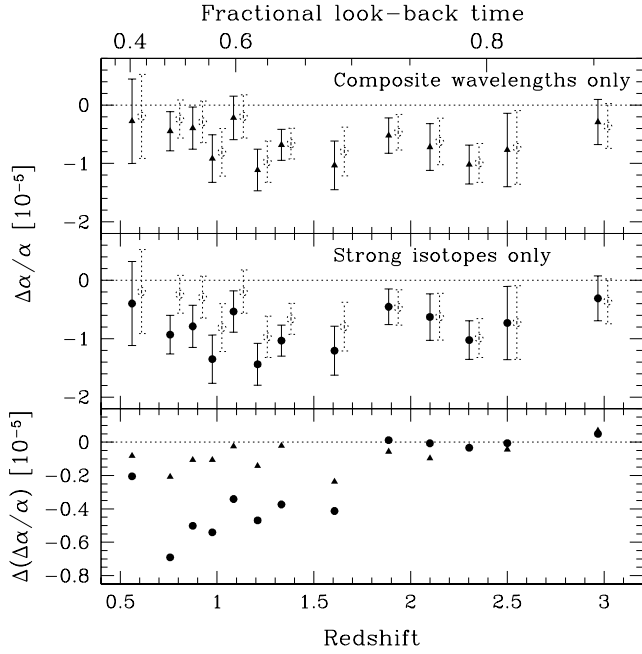


Figure 16. Upper limits on the effects of differential isotopic saturation and isotopic abundance evolution. The top panel compares the binned values of α derived using only the composite laboratory wavelengths (solid triangles) from Table 2 and the values from the raw sample (dotted circles, slightly shifted for clarity). The solid circles in the middle panel are derived using only the isotopic components of the Mg I, Mg II and Si II transitions with the highest terrestrial abundance. The lower panel shows the differences between these composite and single isotope values of α and the values from the raw sample.

magnitude of $(\alpha/\alpha)_{\text{comp}} - (\alpha/\alpha)_{\text{iso}} =$ in M01b and find values of $(\alpha/\alpha)_{\text{comp}}$ for the previous low- and high- z samples. The top panel of Fig. 16 compares values of $(\alpha/\alpha)_{\text{comp}}$ (solid triangles) for the total sample with those found using the full isotopic/hyperfine structures (dotted circles). We see that isotopic saturation has only a small effect on α , even for the Mg/Fe II systems at low- z . This is confirmed when comparing the statistics for this test in Table 4 with the values from the raw sample. It is therefore clear that differential isotopic saturation of Fe II transitions is unlikely to have significantly affected our results.

5.5.2 Differential hyperfine saturation

Hyperfine splitting of energy levels occurs only in species with odd proton or neutron numbers (note that most isotopes in Table 5 are even). Different hyperfine components will have different transition probabilities but the composite wavelength of a line will be unchanged by the splitting (i.e. the centre of gravity of the hyperfine components is constant with increased splitting). However, a similar differential saturation effect will occur for the hyperfine components as for the isotopic components discussed in Section 5.5.1.

By far the most prominent hyperfine structure is that of Al III which is clearly resolved in the laboratory experiments of Griesmann & Kling (2000) and which we take into account in our fits to the QSO data (see Section 2.2). The high- z composite wavelength results in Fig. 16 therefore provide an upper limit on the effect of hyperfine saturation effects for all other transitions. The only other known hyperfine structures are those of the ²⁵Mg transitions. These

are so closely separated that they would have a negligible effect on α (especially considering the small effect of differential isotopic saturation in Fig. 16). In M01b we ruled out significant effects on α from saturation effects in other (odd) species due either to their low relative abundances, low magnetic moments or the nature of the ground- and excited-state wavefunctions. All the above arguments imply a negligible effect due to differential hyperfine saturation.

5.5.3 Isotopic abundance variations

We assumed the terrestrial isotopic abundances in Table 5 when fitting Mg and Si absorption lines. However, if the isotopic abundances in the QSO absorbers are different, small apparent shifts in the absorption lines would be introduced, potentially mimicking a non-zero α . This effect will be greatest for changes in the isotopic abundances of Mg I, Mg II and Si II since the mass shift (equation 7) implies these ions will have the largest isotopic separations.

Observations of Mg (Gay & Lambert 2000) and theoretical estimates for Si (Timmes & Clayton 1996) in stars clearly show a decrease in the isotopic abundances with decreasing metallicity. For example, at relative metal abundances $[\text{Fe}/\text{H}] = -1$, ²⁵Mg $g=^{24}\text{Mg}$ $g=^{26}\text{Mg}$ $g=^{24}\text{Mg}$ 0.1 , which is about 30 per cent below terrestrial values (see Table 5). Theoretical estimates suggest even larger decreases (Timmes, Woosley & Weaver 1995). The metallicities of our absorption systems are all likely to be sub-solar: the Mg/Fe II systems (previous low- z sample) have $Z = 0.25-0.0$ (Churchill & Le Brun 1998; Churchill et al. 2000a,b) and the DLAs in the previous high- z sample have $Z = 1.0$ (Prochaska & Wolfe 1999, 2000). Therefore, we expect significantly lower isotopic abundances of ^{25,26}Mg and ^{29,30}Si in our QSO absorption systems.

Considering the above, refitting the QSO spectra using only the strong isotopes of Mg and Si (i.e. ²⁴Mg and ²⁸Si) should place an upper limit on the effect of possible isotopic abundance variations on α . We first demonstrated this test on the previous samples in M01b and have now applied it to the total sample. We find similar results.

Our new results, $(\alpha/\alpha)_{\text{iso}}$ (solid circles), are compared with the values from the raw sample (dotted circles) in the middle panel of Fig. 16. The lower panel also shows the size of the correction, $(\alpha/\alpha)_{\text{comp}} - (\alpha/\alpha)_{\text{iso}}$. Fig. 16 clearly demonstrates that strong isotopic abundance evolution in Mg and Si can not explain our results. Indeed, α becomes more negative when we remove this potential systematic effect. Note that removing ^{25,26}Mg affects only the low- z Mg/Fe II systems whereas removing ^{29,30}Si affects only the high- z points. The largest effect is for the low- z Mg/Fe II systems. This is expected because (a) the isotopic separations for Mg transitions are larger than those for Si transitions (equation 7), (b) the relative terrestrial abundances of ²⁵Mg and ²⁶Mg are larger than ²⁹Si and ³⁰Si (Table 5) and (c) a large number of different species are fitted in the high- z DLAs so a systematic effect in just one species (in this case Si II) is unlikely to significantly affect α .

The above test estimates the maximum effect of strong isotopic abundance evolution for Mg and Si transitions. Although we emphasize that the effect for heavier species should be reduced by the mass shift, we point out that isotopic (and hyperfine) structures for transitions of other species are not known. It is possible that large specific isotopic shifts exist for some transitions. If this is combined with strong isotopic ratio evolution then small apparent

line shifts would be measured in the QSO spectra. However, this possibility is unlikely given the results of removing single transitions or entire species in Section 5.7.1.

One possibility is that the isotopic abundances do not follow the above expected trend based on the Galactic observations and theoretical models. For example, *higher* $^{25,26}\text{Mg}$ abundances in the absorption clouds would mimic $\delta = < 0$ in the low- z Mg/Fe II systems. The results above allow us to estimate the Mg isotopic ratios required to explain the observed $\delta = 0$ at low- z . The approximate shift in δ will be $\delta(\lambda) = \lambda \frac{\Delta A}{A}$ where $\frac{\Delta A}{A} = \frac{\Delta f}{f}$ is the fractional change in the abundance weighted mean transition wavenumber. Applying this relation to the test results above, we find that the proportionality constant $\delta = 12.2$ using an average $\delta(\lambda) = 0.445 \times 10^{-5}$ (from Table 4) and $\frac{\Delta A}{A} = 3.6 \times 10^{-7}$, the fractional difference between the ^{24}Mg II and composite Mg II 2796 wavenumbers. To shift $\delta = 0$ to an average of zero in the low- z sample, we require $\delta(\lambda) = +0.539 \times 10^{-5}$. Using the just derived, this implies $\frac{\Delta A}{A} = 4.4 \times 10^{-7}$ which could be achieved if the $(^{25}\text{Mg}+^{26}\text{Mg})/^{24}\text{Mg}$ abundance ratio is 0.58 in the absorption clouds (compared to the terrestrial value of 0.27).

5.5.4 Hyperfine level population variations

Once again, consider the prominent hyperfine structure of the Al III transitions. If the populations of the ground-state hyperfine levels are not equal in the absorption clouds, as they are in the laboratory measurements of Griesmann & Kling (2000), we would measure small apparent shifts for the Al III transitions. In M01b we pointed out that a lower bound on the relative population is set by interaction with CMB photons, $\exp[-h\nu/k_B T_{\text{CMB}}(z)]$, where $\nu = 0.5 \text{ cm}^{-1}$ is the hyperfine splitting for the Al III 1854 and 1862 transitions. At $z_{\text{abs}} = 2.0$, the relative population is 0.9, leading to a shift in the line centroid of 0.01 cm^{-1} ($5 \times 10^4 \text{ \AA}$). This corresponds to $\delta = +1 \times 10^{-5}$ for the Al III lines alone. Clearly, including other transitions will reduce the effect on δ for a particular system.

Two caveats significantly lessen concern in this case: (i) collisional excitation processes should drive the relative populations to equality; (ii) removing either or both of the Al III transitions from our analysis has a very small effect on δ (see Section 5.7.1). We therefore consider systematic errors from variations in the hyperfine level populations to be negligible.

5.6 Atmospheric dispersion effects

Below we describe how atmospheric dispersion could have distorted the wavelength scale and instrumental profile (IP) of the QSO spectra. This was the largest potential systematic effect identified in M01b for the previous samples. We model the *potential* effects on our QSO spectra in Section 5.6.1, significantly improving the model in M01b. We search for such effects in the QSO data in Section 5.6.2, finding that *the data themselves suggest negligible effects on δ from atmospheric dispersion*.

5.6.1 Modelling possible distortions from atmospheric dispersion

The Keck/HIRES was only fitted with an image rotator in 1996 August. Therefore, prior to this time, the spectrograph slit could not be held perpendicular to the horizon during observations and so the

atmosphere will have dispersed QSO light with some component across the slit (see figure 5 of M01b). All of the 27 absorption systems in the previous low- z sample were observed before 1996 August. Similarly, 11 systems in the previous high- z sample and half (39) of the new sample were observed ‘pre-rotator’. Therefore, for the total sample, 77 of the 128 absorption systems could be affected by atmospheric dispersion effects.

Before the image rotator was installed, the angle of the Keck/HIRES slit to the vertical, θ , was directly related to the zenith angle by $\theta = 90^\circ - \alpha$. That is, the slit lies with its axis along the horizon at $\alpha = 90^\circ$. The component of atmospheric dispersion along the spectral direction of the slit (i.e. across its axis) therefore increases with increasing α because atmospheric dispersion *and* increase with α . This will lead to two effects on the QSO wavelength scale:

(i) Compression. Due to the angular separation of different wavelengths as they enter the spectrograph, the QSO spectrum will be distorted relative to the ThAr calibration frames. Consider two wavelengths, $\lambda_2 > \lambda_1$, entering the spectrograph slit separated by an angle α in the vertical direction. The spectral separation of the two wavelengths in the extracted, calibrated spectrum will be

$$\Delta\lambda = \lambda_1 \frac{a \sin \alpha}{\lambda_1} ; \quad (13)$$

where a is the CCD pixel size in angstroms and λ_1 is the projected slit width in arcseconds per pixel (for HIRES, $\lambda_1 = 0.287 \text{ per pixel}$). We checked the accuracy of this equation with ZEMAX models of the Keck/HIRES provided by S. Vogt. If $\alpha \ll 0$ then the spectral separation between any two wavelengths will decrease, i.e. the spectrum is compressed⁹. If α is due to atmospheric dispersion then it is a function of the atmospheric conditions and can be estimated using the refractive index of air at the observer and the zenith angle of the QSO (e.g. Filippenko 1982). Note that equation 13 assumes that the seeing profiles at λ_1 and λ_2 are not truncated by the slit edges.

(ii) Wavelength dependent IP asymmetry. If tracking errors or seeing effects do cause profile truncation at the slit edges then the truncation will be asymmetric and this asymmetry will be wavelength dependent. For example, the optical design of Keck/HIRES is such that a blue spectral feature will have its red wing truncated and a red feature will be truncated towards the blue. The asymmetry and the severity of its wavelength dependence will increase with increasing α and with λ (and therefore, α). Note that when we centroid absorption features in the QSO spectra, we will find larger wavelength separations due to this effect, i.e. a positive term is effectively added to the right-hand-side of equation 13.

For the low- z Mg/Fe II systems, these two effects will have an opposite effect on δ : the compression will produce $\delta = < 0$ and the wavelength dependent asymmetry will result in $\delta = > 0$. It is important to note that both effects rely mainly on the same parameters for each observation (i.e. α and λ) and so their relative strength is fixed by our model. The one free parameter is the seeing, which determines the strength of the wavelength asymmetry effect and not the compression effect. We discuss this below.

For each QSO observed without the image rotator we have calculated an effective seeing profile at the spectrograph slit. In

⁹ Note that in M01b we argued that this effect amounted to an expansion of the spectrum rather than a compression. The change in sign here is due to the optics of the CCD camera on Keck/HIRES which reverses the image on the CCD (T. Bida & S. Vogt, private communication). This has now been checked with ZEMAX models of the HIRES.

general, each QSO spectrum is the combination of several exposures and each exposure was taken at a different λ . For each exposure we assume typical observing conditions at the telescope¹⁰ and use the mean value of σ calculated from the recorded image headers to obtain the relative angular separations, θ , between all observed wavelengths. Then, to reconstruct the full dispersion pattern relative to the slit edges, we assumed that light of wavelength $\lambda = 5500 \text{ \AA}$ was centred on the slit axis. This corresponds to the mean wavelength of the response curve for the acquisition camera used to guide Keck/HIRES on the QSO.

For each exposure we assumed a seeing of $\text{FWHM} = 0.75''$ to produce a Gaussian intensity profile at the slit for each observed wavelength. Although this is a realistic assumption, we have no detailed information about the seeing conditions for each observation¹¹. Tracking errors will broaden the intensity profile so the above assumption is effectively a conservative one: if $\text{FWHM} > 0.75''$ then the effect of wavelength dependent IP asymmetry on α will reduce because each wavelength will illuminate the slit more uniformly.

For each QSO observation and at each observed wavelength we average the slit intensity profiles for all exposures. For each observed wavelength (i.e. each observed MM transition) a high S/N, high spectral dispersion synthetic spectrum is constructed based on the Voigt profile fits to the QSO data. We convolve each spectrum with the corresponding intensity profile, truncated by the slit edges, and then we convolve with a Gaussian instrumental response of width $\text{FWHM} = 2.2 \text{ km s}^{-1}$ (Valenti et al. 1995). We vary this parameter slightly depending on the observed wavelength so as to ensure constant velocity resolution to match the real QSO data. Finally, we re-sample the simulated spectra to match the real QSO spectral dispersion.

The above procedure provides synthetic QSO spectra with $\alpha = 0$ but which contain effects due to our model of atmospheric dispersion. We fit these spectra and determine $(\alpha)_{\text{ad}}$, an estimate of the effect of atmospheric dispersion on the values of α derived from the real QSO spectra. The results are plotted in the top panel of Fig. 17 for the 77 systems observed without the image rotator. In the low- z Mg/Fe II systems, atmospheric dispersion causes $\alpha < 0$ (i.e. the compression effect dominates the wavelength dependent IP asymmetry effect) and so, once the effect is modelled and removed, α increases. At high z not all values of α react the same way to atmospheric dispersion since different transitions are fitted in each absorption system. However, on average, the high- z values of α decrease after removing atmospheric dispersion effects.

The middle panel of Fig. 17 shows the corrected values of α , i.e. $(\alpha)_{\text{adc}} = (\alpha)_{\text{ad}}$ (solid squares), including those systems not affected by atmospheric dispersion effects [$(\alpha)_{\text{ad}} = 0$, open squares]. The lower panel compares the binned values of $(\alpha)_{\text{adc}}$ with the raw values from Fig. 6. Clearly, atmospheric dispersion effects (as modelled above) can not explain our results. Indeed, on average, the overall compression of the wavelength scale has an *opposite effect on the low- z and high-*

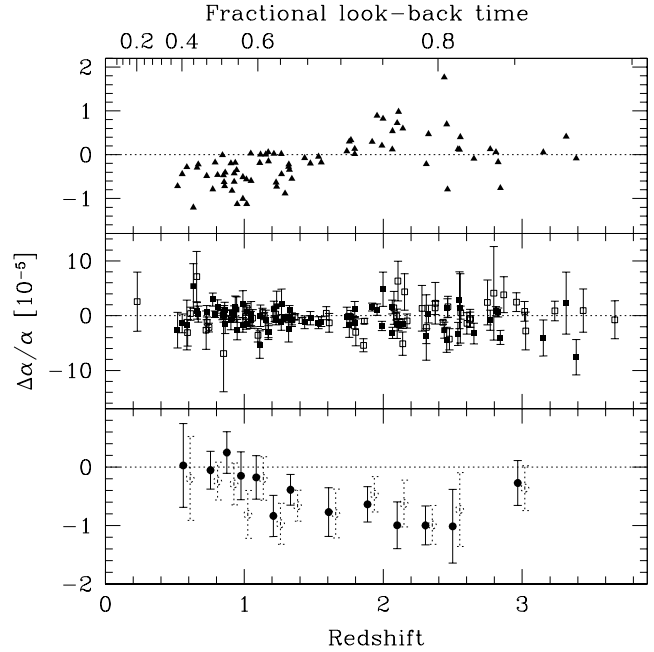


Figure 17. Correcting for potential atmospheric dispersion effects. The upper panel shows values of $(\alpha)_{\text{ad}}$ derived from simulated spectra with our model for atmospheric dispersion applied. We have corrected the relevant raw values of α in the middle panel (solid squares) which also shows the unaffected raw values (open squares). The lower panel compares the binned values from the middle panel (solid circles) with those of the raw sample (open circles). The new overall weighted mean is $\alpha = (0.46 \pm 0.10) \times 10^{-5}$.

Table 6. Comparison of weighted mean values of α for the pre- and post-rotator systems.

Sample	Pre-rotator		Post-rotator	
	N_{abs}	α	N_{abs}	α
Total sample (Fig. 20, middle panel)				
low- z	52	0.60 ± 0.16	22	0.45 ± 0.20
high- z	25	0.39 ± 0.26	29	0.83 ± 0.23
Total	77	0.54 ± 0.14	51	0.62 ± 0.15
New sample only (Fig. 20, lower panel)				
low- z	22	0.67 ± 0.25	22	0.45 ± 0.20
high- z	17	0.77 ± 0.33	17	0.50 ± 0.31
Total	39	0.71 ± 0.20	39	0.46 ± 0.17

z systems. This is further borne out by the simulations in Section 5.7.2 (see Fig. 23).

In summary, it is clear that atmospheric dispersion effects can not explain the observed values of α . Assuming an effective seeing, our model of atmospheric dispersion provides a realistic upper limit to the potential effects on α . Additional tracking/guiding errors will significantly reduce these effects by smearing the QSO light more evenly across the spectrograph slit.

5.6.2 Evidence for atmospheric dispersion effects?

If atmospheric dispersion significantly affects α then, from the discussion above, we expect to find a correlation between α and the zenith distance, z . We search for a such a correlation in

¹⁰ We assumed the following observational parameters in our atmospheric dispersion model: temperature = 280 K, atmospheric pressure = 600 mbar and relative humidity = 10 per cent.

¹¹ In principle, one could find a reliable estimate of the seeing for each exposure by integrating the object profile in the spatial direction along the echelle orders. In general, we did not have access to the un-extracted, 2-dimensional object exposures and so could not perform such an analysis.

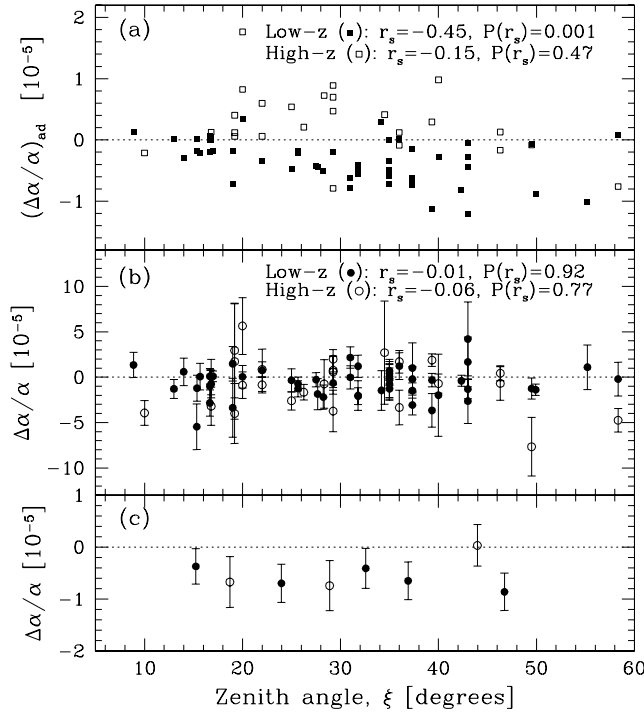


Figure 18. Is α correlated with zenith angle? (a) The estimates of the effect of atmospheric dispersion on α as a function of the mean zenith angle, ξ , for each observation. The Spearman rank correlation coefficient, r_s , and associated probability, $P(r_s)$, indicate a clear anti-correlation for the low- z systems but no clear correlation for the high- z systems. (b) The real raw values of α . No correlation is seen for either the low- or high- z systems. (c) A binning of the real values to clarify the lack of correlation with ξ .

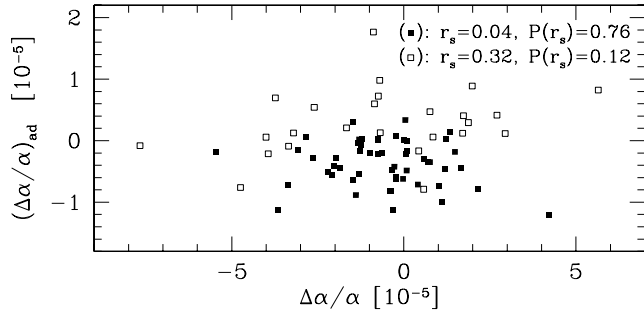


Figure 19. Is $(\Delta\alpha/\alpha)_{\text{ad}}$ correlated with $\Delta\alpha/\alpha$? The Spearman rank correlation coefficient and associated probability indicate no clear correlation for the low- z systems (solid squares). A weak correlation may exist in the high- z systems (open squares) but only at low significance.

Fig. 18. In panel (a) we plot the estimates of $(\Delta\alpha/\alpha)_{\text{ad}}$ from the previous section versus the mean value of α for each absorption system affected by atmospheric dispersion. The Spearman rank correlation coefficient, r_s , and associated probability, $P(r_s)$ ¹², indicate a clear anti-correlation for the low- z systems (solid squares). However, we see no evidence for such a correlation in the real low- z values which are shown in panel (b). Panel (c) shows a binning of the results for clarity. This indicates that atmospheric dispersion has had no significant effect on the raw values of α . For the high-

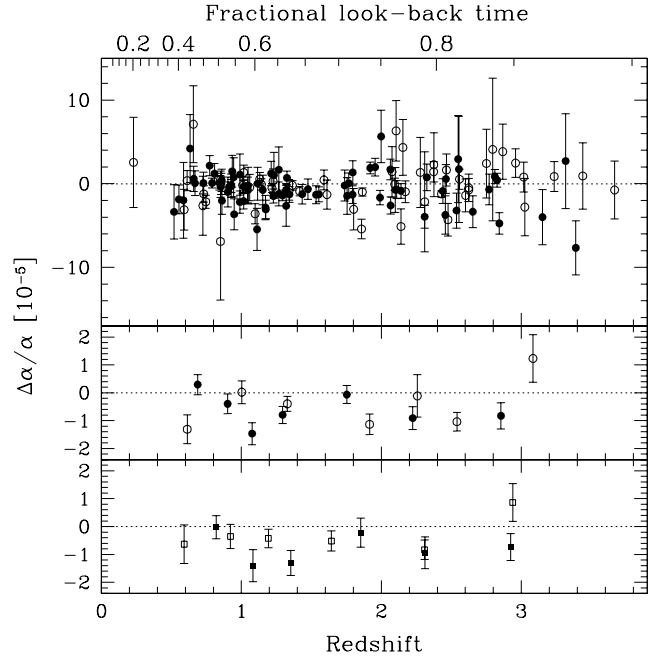


Figure 20. Comparison of the pre- and post-rotator systems. The upper panel compares raw values of α for the pre-rotator (solid circles, 77 points) and post-rotator (open circles, 51 points) samples. The weighted means are consistent: $\alpha = (0.54 \pm 0.14) \times 10^{-5}$ and $\alpha = (0.62 \pm 0.15) \times 10^{-5}$ respectively. The middle panel bins the results in the same fashion as for the main results in Fig. 6. We see no evidence for a significant systematic effect due to atmospheric dispersion. The lower panel compares the pre-rotator (solid squares, 39 points) and post-rotator (open squares, 39 points) subsamples of the new sample alone. Again, we see no evidence for the atmospheric dispersion effect. Table 6 presents the weighted mean values of α .

z systems, we also see no correlation between α and ξ , since the upper panel shows no clear correlation for the estimates of $(\Delta\alpha/\alpha)_{\text{ad}}$, one cannot take this as evidence against atmospheric dispersion. One also expects a correlation between $(\Delta\alpha/\alpha)_{\text{ad}}$ and α if atmospheric dispersion effects are significant. However, in Fig. 19 we see no clear evidence for such a correlation for either the low- or high- z samples (solid and open squares respectively).

We may also test for atmospheric dispersion effects by comparing the value of α for the (77) pre- and (51) post-rotator values of α . In the top panel of Fig. 20 we identify these subsamples and plot binned values in the middle panel. There is no discrepancy between the pre- and post-rotator samples. This is confirmed in Table 6 where we compare the weighted mean values of α . Even for the low- z systems, which should be most susceptible to atmospheric dispersion effects, we see no evidence for a discrepancy. We also consider the new sample separately in the lower panel of Fig. 20 where exactly half of the systems are pre-rotator observations. Again, in Table 6, the weighted mean values of α are consistent.

To summarize this section, we emphasize that the QSO data themselves suggest that atmospheric dispersion had an insignificant effect on α . No correlation between α and the zenith angle of the QSO observations is observed (Fig. 18) and the pre- and post-rotator samples give completely consistent results (Fig. 20 and Table 6).

¹² $P(r_s)$ is the probability that $|r_s|$ could have been exceeded by chance.

5.7 Line-removal tests

A non-zero β manifests itself as a distinct pattern of line shifts (see Fig. 1). For a given absorption system, with a given set of fitted transitions, we can remove one or more transitions and still obtain a well-constrained value of β . In the absence of systematic errors associated with the transition removed or with the wavelength scale of the QSO spectra, β should not change systematically over all absorption systems. Removing a single transition or distinct groups of transitions from our analysis therefore allows us to search for systematic errors without specific knowledge of their origin. Note that removing one or more transitions will result in a slightly modified estimate of the velocity structure, revising the estimate of β for each system. However, this will have a random effect on β ; the real question is, how robust are the values of β , averaged over the entire sample, to this line removal process?

Below we construct three different line removal tests, each sensitive to different types of systematic errors.

5.7.1 Single transition and species removal

Removing a single transition (e.g. Mg II λ 2796) from the fits to the QSO data provides a direct means to search for systematic errors due to systematic line blending (Section 5.2.2), isotopic and hyperfine structure effects (Section 5.5) and large errors in the measured laboratory wavelengths in Table 2. Removing entire species (e.g. all transitions of Si II) is also a test for isotopic and hyperfine structure effects.

Given an absorption system, with a certain set of fitted transitions, we only remove transitions that *can* be removed. To clarify this, consider removing the Mg II λ 2796 transition. For the low- z Mg/Fe II systems, a well-constrained value of β can only be obtained when at least one Mg line is fitted since there is only a small difference between the q coefficients for the different (low- z) Fe II transitions (see Fig. 1). Therefore, if the only anchor line present is Mg II λ 2796 then we can not remove it from the system. Similarly, we only remove the entire Mg II species if the Mg I λ 2852 line is fitted.

We presented the results of removing single transitions and entire species for the previous samples in M01b. In Fig. 21 we present line removal results for the total sample. The transition/species removed is given on the vertical axis together with the number of systems, n , where removal was possible. The left panel compares the weighted mean value of β before removing the transition/species (dotted error bar) with that obtained afterwards (solid error bar) for these n systems. The right panel shows the effect of removing the transition/species on the weighted mean β for the sample as a whole (i.e. including those systems where the transition in question could not be removed). Raw values of β are used in all cases (i.e. the 1 σ errors returned from VPFIT are not increased to take account of extra scatter in high- z sample).

Fig. 21 provides no evidence to suggest that systematic errors associated with any one transition or species have significantly affected β . This strongly suggests that isotopic/hyperfine saturation or evolution effects are not important for the transitions of interest. This is particularly important information for the majority of transitions for which the isotopic structures are not known (see Section 5.5). The line removal results also confirm that random and systematic blending with unidentified transitions has a negligible effect on β .

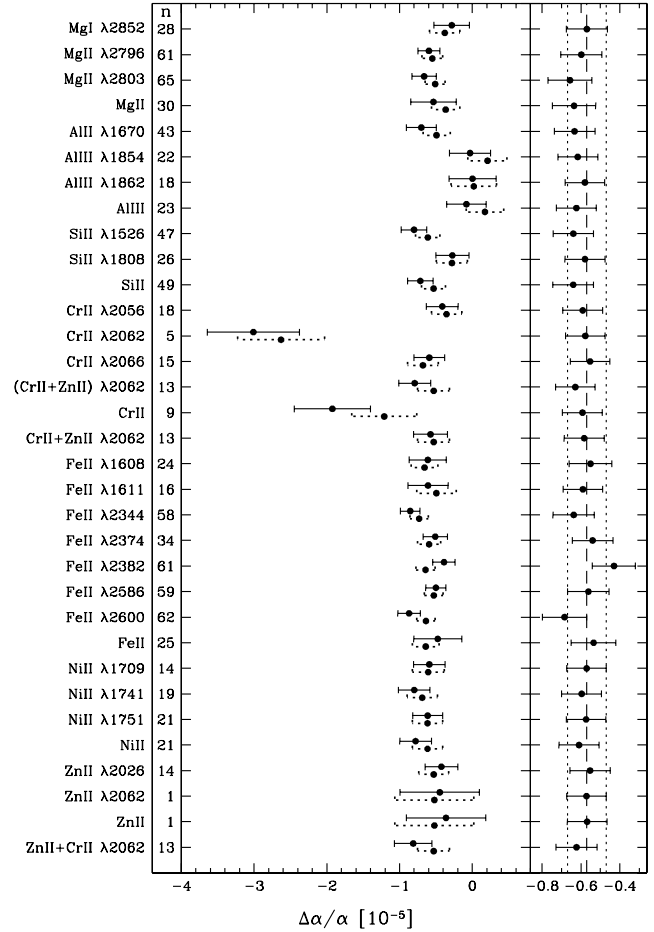


Figure 21. Single transition and species removal. The left panel compares the raw values of β before (dotted error bar) and after (solid error bar) line removal. The transitions or species removed are listed on the left together with the number of systems, n , for which line removal was possible. The right panel shows the impact of line removal on the value of β for the entire sample. The vertical lines indicate the raw weighted mean value of β (dashed line) and 1 σ error range (dotted lines). Note that some confusion may arise due to the occasional blending of the Cr II and Zn II λ 2062 lines: ‘(Cr II + Zn II) λ 2062’ refers to cases where both transitions had to be removed simultaneously; ‘Cr II + Zn II λ 2062’ refers to cases when all Cr II transitions were removed along with the blended Zn II λ 2062 line; a similar definition applies to ‘Zn II + Cr II λ 2062’; ‘Cr II’ and ‘Zn II’ refer only to removal of the Cr II and Zn II species in cases where the Cr II and Zn II λ 2062 lines were not blended.

5.7.2 High- z compression test

As previously noted, the arrangement of the q coefficients for the low- z Mg/Fe II systems (see Fig. 1) implies that a compression of the wavelength scale will systematically lead to $\beta < 0$. The dependence of β on the q coefficients is considerably more complicated for the high- z systems: a compression of the wavelength scale will have a different effect on each value of β depending on which transitions are fitted. That is, compression is not degenerate with $\beta = 0$ at high- z . If compression is responsible for the observed $\beta < 0$ at low z , can evidence for it be found in the high- z absorption systems?

We search for compression in the high- z sample by fitting combinations of transitions for which the q coefficients are arranged in a similar way to those for the low- z Mg/Fe II systems.

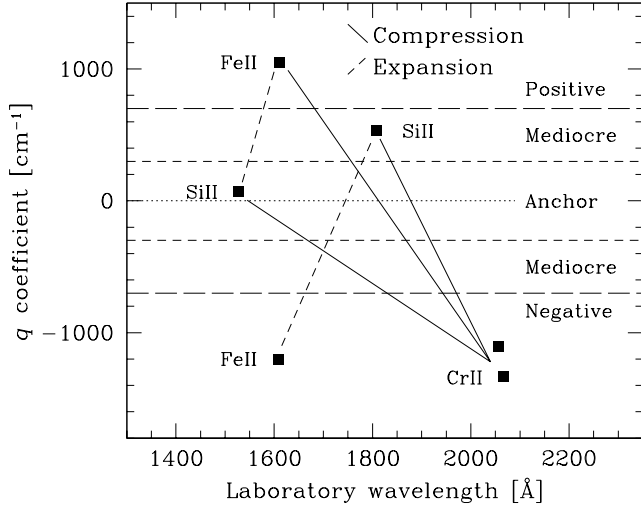


Figure 22. The high- z compression test. A compression of the spectrum will systematically produce $q < 0$ in a high- z absorption system if only certain combinations of transitions (solid diagonal lines) are fitted simultaneously. This mimics the situation for the low- z Mg/Fe II absorption systems and allows us to search for a compression-type systematic effect in the high- z systems. Combinations of transitions which will give $q > 0$ for an expansion of the spectrum can be selected in a similar way (dashed diagonal lines).

For example, consider a system where the following transitions are present in the QSO spectrum: Si II 1526 & 1808, Fe II 1608 & 1611 and Cr II 2056 & 2066. The arrangement of q coefficients for such a system is shown in Fig. 22. Fitting the Si II 1526 and Cr II transitions will yield $q < 0$ if a compression of the spectrum exists. Note that several different combinations could be used to the same effect, as indicated by solid diagonal lines. We treat such cases separately in our analysis since the lower wavelength transitions (i.e. Si II 1526 & 1808 and Fe II 1608) are of different q -type. The values of q and the 1σ errors in these separate cases will not be independent. Note also that we can form combinations of transitions which mimic $q < 0$ for an *expansion* of the spectrum.

From the high- z sample, 47 systems contribute 76 different, but not independent, combinations to the compression sample. Similarly, 59 systems contribute 126 combinations to the expansion sample. In Table 7 we calculate the raw values of the weighted and unweighted means for each sample both before and after removing transitions to form the compression and expansion combinations. Note that the number of compression combinations formed in a given absorption system is the number of times that system contributes to the pre-removal values. Table 7 shows no clear evidence for compression (or expansion) in the high- z sample. However, the weighted and unweighted means are not adequate statistics because each absorption system can contain many combinations. Furthermore, the pre- and post-removal values and their 1σ errors are not independent of each other. Also of note are the large errors in the unweighted mean post-removal values, indicating a large scatter in the results and, therefore, that the weighted means are unreliable.

To properly interpret results from the compression test, a comparison must be made with detailed simulations of the QSO data. We synthesized each absorption system from the Voigt profile fit to the real QSO data, adding Gaussian noise appropriate to the measured S/N. From each synthetic spectrum we constructed 3 different simulations:

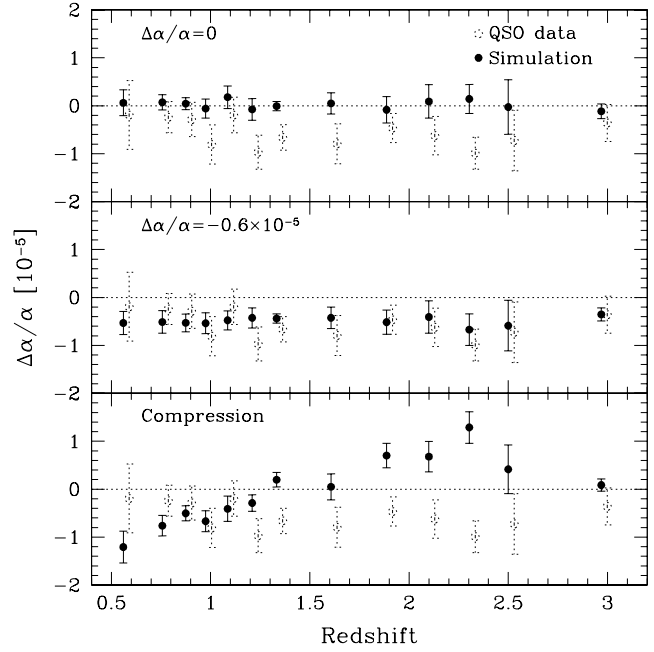


Figure 23. q from simulations of the QSO spectra. The weighted mean from 20 simulations (solid circles) is compared with the real raw values (dotted circles, shifted for clarity) in each panel. The rms from the simulations is represented by the error bar. The upper panel has no input value of q whereas $q = 0.6 \times 10^{-5}$ was introduced into the spectra for the middle panel. Note that we recover the input values and that the rms error bars match the 1σ errors in the real data. A compression was introduced into the spectra for the lower panel (equation 14) to allow interpretation of the high- z compression and q -type removal test results.

- (i) $q = 0$. No line shifts were introduced into the synthetic spectra.
- (ii) $q = 0.6 \times 10^{-5}$. Each transition in the synthetic spectrum was shifted according to this value of q which corresponds to the raw weighted mean value measured in the real QSO data.
- (iii) Compression. The synthetic spectrum was compressed according to

$$\lambda^0 = C(\lambda_c - \lambda_c^0); \quad (14)$$

where λ^0 is the initial wavelength of a given pixel and λ^c is the new value obtained by compressing the spectrum about a central wavelength, λ_c , by a factor C . This mimics the compression effect of atmospheric dispersion, as described by equation 13. Thus, we chose $\lambda_c = 5500 \text{ Å}$ as representative. In order to produce $q = 0.6 \times 10^{-5}$ in the low- z simulated spectra, we used $C = 4 \times 10^{-6}$.

We ran 20 simulations of each absorption system, obtaining values of q for each of the 3 cases above. The results are compared with the real, raw sample in Fig. 23. Note that (i) we recover the input values of q for the $q = 0$ and $q = 0.6 \times 10^{-5}$ cases and (ii) the compression simulation shows a similar behaviour to that of the atmospheric dispersion calculation in Fig. 17, confirming that simple distortions of the wavelength scale should have had an opposite overall effect on the high- z systems compared to the low- z systems.

We have applied the high- z compression test to the simulations for each of the above 3 cases. The results are shown in the lower three panels of Fig. 24, binned for clarity. The error bars on

Table 7. Coarse results from the high- z compression test. Columns 4 and 5 show the raw values of the weighted and unweighted mean $\Delta\alpha/\alpha$ (in units of 10^{-5}) for the relevant absorption systems before removing the transitions. Each absorption system may contribute many times to these values, depending on how many compression/expansion combinations can be formed from the fitted transitions. Columns 6 and 7 give the weighted and unweighted mean after transitions are removed to produce the compression/expansion combinations. Note the large errors in the post-removal unweighted means. Other caveats of interpreting this table are discussed in the text.

Sample	N_{abs}	Combinations	Pre-removal				Post-removal			
			\bar{h}	\bar{i}_w	\bar{h}	\bar{i}	\bar{h}	\bar{i}_w	\bar{h}	\bar{i}
Compression	47	76	0.74	0.16	0.88	0.34	1.56	0.31	0.82	0.86
Expansion	59	126	0.52	0.10	0.34	0.26	0.38	0.17	0.93	0.72

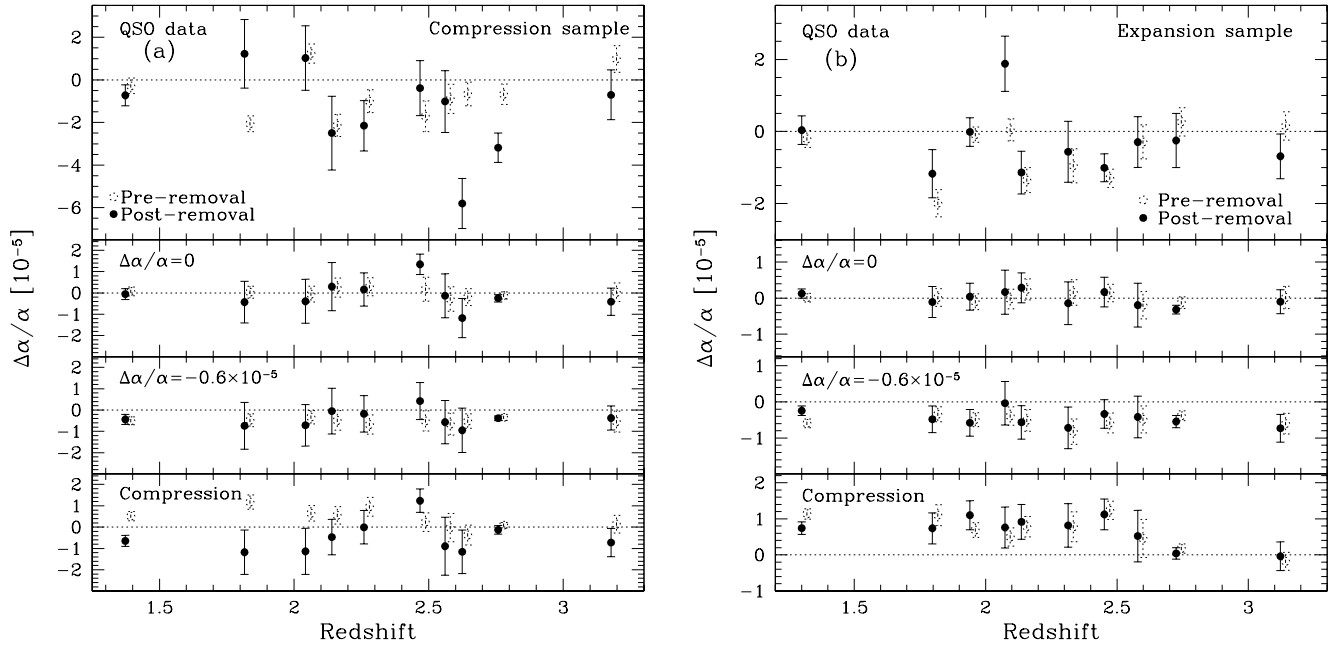


Figure 24. Detailed results of the high- z compression test for the QSO data (upper panels) and simulations (lower 3 panels). The error bars for the simulations represent the rms from 20 synthetic spectra. **(a)** Compression sample. Each panel shows binned values of $\Delta\alpha/\alpha$ before and after transitions are removed to form the 76 compression combinations. The bottom panel shows that the compression sample is sensitive to the synthetic compression introduced to the simulated spectra. No clear trend is seen in the real QSO data due to the large scatter in the post-removal values (see text for discussion). **(b)** Expansion sample. 126 combinations contribute to the binned values of $\Delta\alpha/\alpha$ shown. No significant difference is observed between the pre- and post-removal values in any of the simulations. The lower panel implies that the expansion sample is surprisingly insensitive to simple systematic errors. Significant scatter is also observed in the post-removal QSO results.

the simulated pre- and post-removal values represent the rms from the 20 simulations of each absorption system. For the $\Delta\alpha/\alpha = 0$ and $\Delta\alpha/\alpha = 0.6 \times 10^{-5}$ simulations, note that $\Delta\alpha/\alpha$ does not change systematically after removing transitions to form the compression and expansion samples. As expected, the compression of the synthetic spectra causes the post-removal values of the compression sample (bottom panel of Fig. 24a) to shift towards more negative values. However, the compression simulation for the expansion sample (bottom panel of Fig. 24b) reveals this sample to be surprisingly insensitive to the artificial compression of the spectra.

The top panels of Fig. 24 compare the pre- and post-removal values of $\Delta\alpha/\alpha$ for the real QSO data. The results are binned in the same way as the simulations but the error bars represent the 1 error in the weighted mean of values within each bin. Of particular note is the large scatter in the post-removal values compared to the size of the rms error bars in the simulations. The scatter is also large compared to the post-removal shift in $\Delta\alpha/\alpha$ seen in the compression simulations. We explained the origin of the extra scatter at

high- z in Section 4.2 and formed the fiducial sample by adding an additional random error to the systems likely to be most strongly affected. We expect this scatter to significantly increase as transitions are removed from the fit, as in the present case. The degree of extra scatter is, to some extent, represented by the large uncertainties in the unweighted means presented in Table 7. These values should therefore be far more reliable in such circumstances.

It is therefore clear that the potential power of the compression test (demonstrated in the bottom panel of Fig. 24a) is undermined by the extra scatter in the high- z values. Unfortunately, one can draw no conclusions about potential systematic errors from the compression test without a significant increase in high- z sample size.

5.7.3 High- z α -type removal

If simple systematic errors are responsible for our measured non-zero $\Delta\alpha/\alpha$, it is surprising that $\Delta\alpha/\alpha$ is so consistent between

Table 8. Coarse results of the high- z α -type removal test. Columns 3 and 4 show the raw weighted and unweighted mean values of $\alpha = \langle \alpha \rangle$ (in units of 10^{-5}) for the 26 relevant absorption systems before removing the transitions (the first three rows necessarily have the same value). Columns 5 and 6 give the weighted and unweighted mean after transitions of the specified α -type are removed. Note that the pre- and post-removal values of $\alpha = \langle \alpha \rangle$ and the 1σ errors are not independent of each other. Also note the large errors in the post-removal unweighted means. A detailed comparison must refer to simulations of the QSO data (see Fig. 25).

α -type removed	N_{abs}	Pre-removal				Post-removal			
		$\alpha = \langle \alpha \rangle_w$	$\alpha = \langle \alpha \rangle$	$\alpha = \langle \alpha \rangle_w$	$\alpha = \langle \alpha \rangle$	$\alpha = \langle \alpha \rangle_w$	$\alpha = \langle \alpha \rangle$	$\alpha = \langle \alpha \rangle_w$	$\alpha = \langle \alpha \rangle$
Anchors	26	0:65	0:18	0:68	0:55	0:88	0:21	0:88	0:46
Positive-shifters	26	0:65	0:18	0:68	0:55	1:21	0:52	0:25	1:39
Negative-shifters	26	0:65	0:18	0:68	0:55	0:63	0:34	1:89	1:28
Mediocre-shifters	21	0:48	0:22	0:39	0:59	0:41	0:22	0:26	0:72

the low- and high- z samples. The lower panel of Fig. 23 explicitly demonstrates this. It would also be surprising if we were to take subsets of the QSO absorption lines, grouped according to the sign and magnitude of α , and find consistent values of $\alpha = \langle \alpha \rangle$. We can apply such a test to the high- z sample only, since it contains transitions with several distinct types of α coefficient (see Fig. 1).

We have applied this high- z α -type removal test to 26 absorption systems. These contained at least one transition of each of the highly delineated α -types, i.e. anchors, positive- and negative-shifters. 21 of these systems also contain at least one mediocre-shifter. If a low-order distortion of the wavelength scale causes the observed non-zero $\alpha = \langle \alpha \rangle$, removing all transitions of one α -type may result in a significant change in $\alpha = \langle \alpha \rangle$. Table 8 compares the weighted and unweighted mean values of $\alpha = \langle \alpha \rangle$ before and after α -type removal. Although removing the anchors, mediocre-shifters and negative-shifters produces only small changes in $\alpha = \langle \alpha \rangle$, removing the positive-shifters seems to cause a significant change. However, two important caveats should be noted: (i) the pre- and post-removal values of $\alpha = \langle \alpha \rangle$ are not independent of each other. This also applies to the 1σ error bars. (ii) After removing the positive- and negative-shifters, the errors in the unweighted mean values are large, indicating a large scatter in $\alpha = \langle \alpha \rangle$. Both these points make the results in Table 8 difficult to interpret. As in the previous section, the unweighted mean values should be far more reliable than the weighted means due to the extra scatter. This is confirmed below.

As for the high- z compression test, comparison with simulations facilitates interpretation of the above results. We have applied the α -type removal test to the 3 simulations described in Section 5.7.2. The results are shown in the lower three panels of Fig. 25, binned for clarity. The error bars on the simulated pre- and post-removal values represent the rms from 20 simulations of each absorption system. Firstly, note the consistency between the pre- and post-removal values for the $\alpha = \langle \alpha \rangle = 0$ and $\alpha = \langle \alpha \rangle = 0.6 \times 10^{-5}$ simulations in panels (b), (c) and (d). Also, in the simulations of compressed spectra, we see that removing the anchor transitions [panel (b)] does not significantly affect the values of $\alpha = \langle \alpha \rangle$. However, the effect is more significant when the positive- and negative-shifters are removed. Overall, we see $\alpha = \langle \alpha \rangle$ decrease when the positive-shifters are removed whereas removing the negative-shifters increases $\alpha = \langle \alpha \rangle$. This illustrates the potential power of the α -type removal test in searching for low-order systematic distortions of the wavelength scale.

The top panels of Fig. 25b, c and d compare the pre- and post-removal results for the real QSO data. The results are binned in the same way as the simulations but the error bars represent the

1σ error in the weighed mean of values within each bin. As for the high- z compression test results in Fig. 24, the results are confused by the significant scatter in the post-removal QSO values. We even observe extra scatter when removing the anchors from the real QSO data. Again, this extra scatter is expected. We also expect it to be worse here than for the compression test since (i) removing the positive- or negative-shifters significantly reduces the sensitivity of the MM method to $\alpha = \langle \alpha \rangle$, (ii) less absorption systems contain all three of the necessary α -types than systems contributing to either the compression or expansion samples and (iii) many combinations of transitions can be used for each absorption system in the compression test. Also, by selecting systems which contain anchors, positive- and negative-shifters, we tend to select systems with transitions of very different line strengths (e.g. transitions of Al II, Cr II and Zn II; see Fig. 1). We explained how this leads to extra scatter in values of $\alpha = \langle \alpha \rangle$ in Section 4.2 and defined a ‘high-contrast’ sample of 22 systems at high- z . 18 of these systems are contained in the sample of 26 systems where α -type removal is possible. The extra scatter is clearly apparent in Fig. 25a which shows the unbinned pre-removal values of $\alpha = \langle \alpha \rangle$ for these 26 systems.

To summarize this section, simulations indicate that removing transitions, grouped according to the magnitude and sign of α , is a potentially powerful test for simple systematic errors in the high- z data. However, the extra scatter in the values of $\alpha = \langle \alpha \rangle$ for the relevant 26 absorption systems precludes any conclusion about the existence or magnitude of such systematic effects.

6 DISCUSSION AND CONCLUSIONS

6.1 Summary of new results

We have used the MM method to analyse 3 samples of Keck/HIRES QSO spectra containing a total of 128 absorption systems over the redshift range $0.2 < z_{\text{abs}} < 3.7$. All 3 samples independently yield consistent, significantly non-zero values of $\alpha = \langle \alpha \rangle$ (Table 4, Fig. 6). Combining the samples gives a weighted mean $\alpha = \langle \alpha \rangle = (0.574 \pm 0.102) \times 10^{-5}$. For systems at $z_{\text{abs}} < 1.8$, the predominant transitions arise from Mg II and Fe II whereas the higher z systems contain a variety of ions and transitions which have a diverse dependence on α . Therefore, if systematic effects were responsible for the observed non-zero $\alpha = \langle \alpha \rangle$, one would expect significantly different values at low- and high- z (Fig. 23). However, we find a similar $\alpha = \langle \alpha \rangle$ in both cases, suggesting that our results are robust.

We identified a source of additional *random* scatter in the values of $\alpha = \langle \alpha \rangle$ for 22 (out of 54) high- z systems, i.e. those for

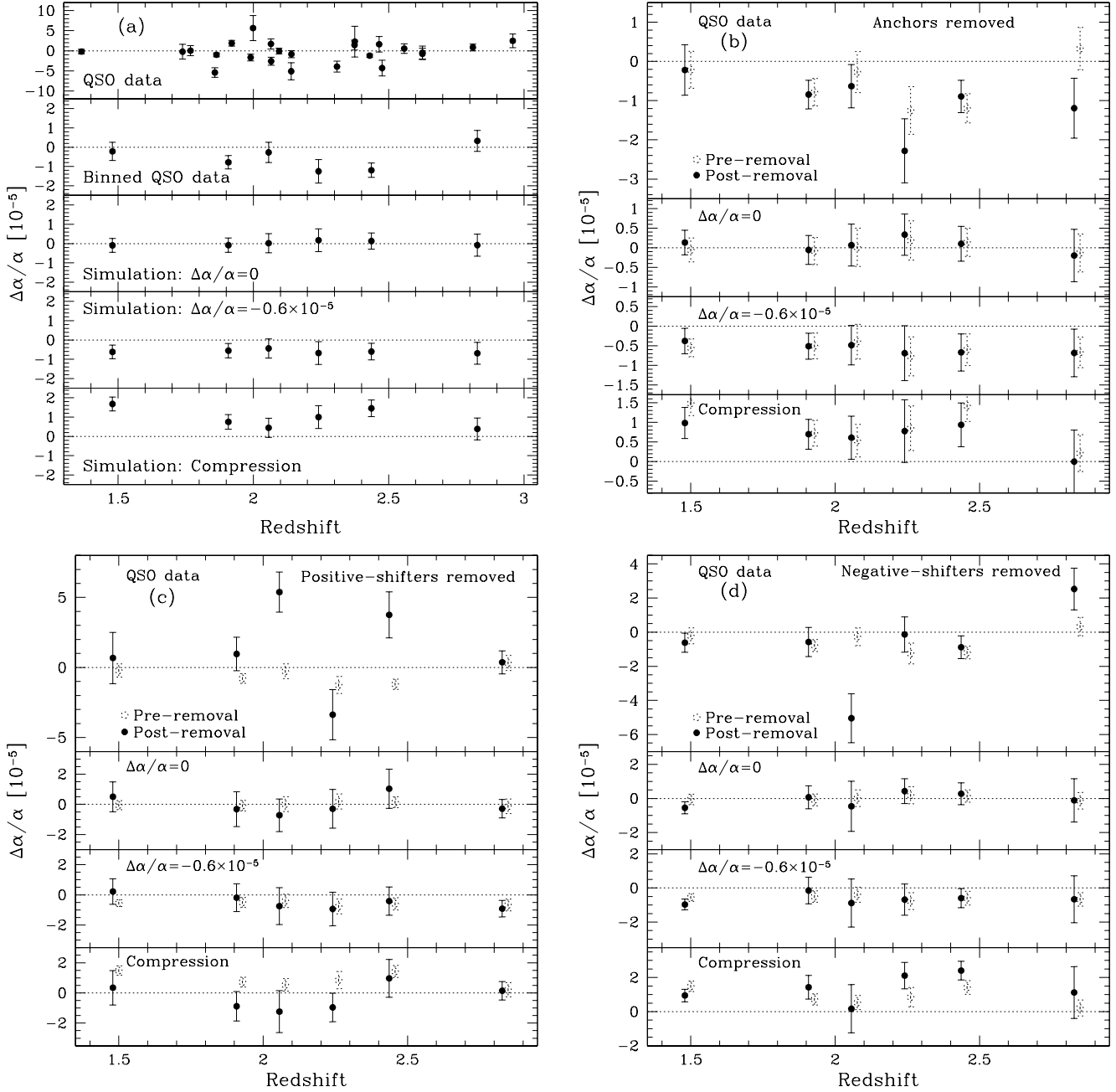


Figure 25. Detailed results of the high- z α -type removal test for the QSO data and simulations (lower 3 panels). The error bars for the simulations represent the rms from 20 synthetic spectra. **(a)** The upper panel shows the values of $\Delta\alpha/\alpha$ for the 26 systems comprising the α -type sample, i.e. those with at least one anchor, positive- and negative-shifter. These data are binned in the next panel. The lower three panels show the weighted mean values of $\Delta\alpha/\alpha$ for the different simulations. These values and the binned QSO data are shown as dotted circles in (b), (c) and (d). **(b)** Anchors removed. The synthetic spectra with artificial compression (lower panel) indicate that removing the anchors should not affect $\Delta\alpha/\alpha$ significantly, even when distortions of the wavelength scale are present. The QSO values also show little deviation after line removal but some extra scatter may exist. **(c)** and **(d)** Positive- and negative-shifters removed. Although the compression simulation reveals a significant change in $\Delta\alpha/\alpha$ upon line-removal, the extra scatter in the post-removal QSO data precludes a firm conclusion about the presence of systematic effects (see text for discussion).

which the fitted transitions have widely differing optical depths. In these systems, the velocity structure is primarily constrained by the low optical depth transitions. Any velocity components too weak to feature in low optical depth transitions may, nevertheless, subtly affect the fitted line positions of nearby velocity components in the high optical depth transitions. We have therefore increased the errors on $\Delta\alpha/\alpha$ for these systems to match the observed scatter.

Our most robust estimate for the overall weighted mean becomes $\Delta\alpha/\alpha = (0.543 \pm 0.116) \times 10^{-5}$, representing 4.7 statistical evidence for a smaller $\Delta\alpha/\alpha$ in the QSO absorption systems (Fig. 8).

If one assumes that $\Delta\alpha/\alpha = 0$ at $z_{\text{abs}} = 0$ then a constant increase in $\Delta\alpha/\alpha$ with time is preferred by the data over a constant offset from the laboratory value: $\Delta\alpha/\alpha = (6.40 \pm 1.35) \times 10^{-16} \text{ yr}^{-1}$ (Fig. 9). However, a bootstrap analysis demonstrates that this pref-

erence has low significance. We find no evidence for dipolar variations from the angular distribution of $\eta = \eta$ (Fig. 10) and no evidence for spatial correlations in η over 0.2–13 Gpc comoving scales from the two point correlation function (Fig. 12).

We have searched for possible instrumental and astrophysical systematic effects which could mimic the above evidence for varying η . As we found in M01b, the two most important of these are due to possible atmospheric dispersion effects and isotopic abundance variations. Sixty per cent of the absorption systems may be affected by the former. However, comparison of the affected and unaffected systems yields no evidence for these effects (Fig. 20). Modelling of atmospheric dispersion and its effect on the QSO spectra indicates that $\eta = \eta$ in the low- z systems should be correlated with the zenith angle of the QSO observations. We observe no such correlation (Fig. 18). Atmospheric dispersion effects clearly can not explain our results. The effect of possible variations in the isotopic ratios is more difficult to estimate. The isotopic abundance trends in low metallicity stellar environments suggest that the $^{25}\text{Mg}/^{24}\text{Mg}$ and $^{29}\text{Si}/^{28}\text{Si}$ ratios will be significantly lower in the QSO absorption clouds. This systematic effect, if present, should have pushed $\eta = \eta$ to positive values. Thus, when it is incorporated into the analysis, $\eta = \eta$ becomes more negative (Fig. 16).

6.2 Comparison with other QSO absorption lines constraints

The only other QSO absorption line method which directly constrains $\eta = \eta$ is the AD method outlined in Section 1.1.1. The MM method constraints in the present work are more than an order of magnitude more precise than the strongest AD method constraints (obtained in Murphy et al. 2001c).

Comparison of H I 21-cm and millimetre-band molecular rotational absorption frequencies constrains variations in $\eta = \eta$, where g_p is the proton g -factor (Drinkwater et al. 1998). This technique suffers from an important systematic error which is difficult to quantify: the millimetre-band and radio continuum emission generally originate from different regions of the background QSO, leading to possible line-of-sight velocity differences between the millimetre-band and H I 21-cm absorption lines. Drinkwater et al. (1998) compared Galactic H I 21-cm and millimetre-band absorption lines to estimate the likely line-of-sight velocity difference, $j v_j = 1.2 \text{ km s}^{-1}$. This corresponds to a systematic effect for a single measurement of $j y = y_j = 0.4 \times 10^{-5}$. This formed the dominant (1 σ) uncertainty in our recent measurements of $y = y$ for two absorption systems (Murphy et al. 2001d): $y = y = (0.20 \pm 0.44) \times 10^5$ for $z_{\text{abs}} = 0.2467$ towards PKS 1413+135 and $y = y = (0.16 \pm 0.54) \times 10^5$ for $z_{\text{abs}} = 0.6847$ towards TXS 0218+357. Carilli et al. (2000) argue that $j v_j$ could be as large as $10\text{--}100 \text{ km s}^{-1}$ on the basis of typical subkiloparsec motions of the ISM. They derive the upper limit $j y = y_j < 1.7 \times 10^{-5}$ for the same two absorption systems.

Comparison of optical and H I 21-cm absorption frequencies constrains variations in $x = x$, where $m_e = m_p$ is the electron-to-proton mass ratio (Wolfe et al. 1976). Cowie & Songaila (1995) obtained $x = x = (0.70 \pm 0.55) \times 10^5$ from the $z_{\text{abs}} = 1.7764$ system towards Q1331+170. However, the effect of line-of-sight velocity differences has not been estimated for the optical/H I comparison but is likely to be at least $j v_j = 1.2 \text{ km s}^{-1}$, as found for the millimetre/H I technique. A statistical sample of $x = x$ and $y = y$ measurements is required to provide reliable constraints and to properly quantify the typical line-of-sight velocity differences. This is currently limited by the small number of sys-

tems known to exhibit both optical/millimetre-band and H I 21-cm absorption (e.g. Curran et al. 2002).

The above constraints on $y = y$ and $x = x$ can only be compared with MM constraints on $\eta = \eta$ if one assumes the constancy of g_p and $m_e = m_p$ respectively. If one suspects variation in then it seems wholly unjustified to assume the constancy of other fundamental parameters like g_p and $m_e = m_p$. Some *model dependent* links between $\eta = \eta$, $x = x$, and $y = y$ and have been studied recently within the paradigm of grand unification (e.g. Langacker, Segrè & Strassler 2002; Dent & Fairbairn 2003; Dmitriev & Flambaum 2003). Langacker et al. (2002) emphasize that the observations should be used to constrain the theory and not *vice versa*.

6.3 Comparison with non-QSO absorption lines constraints

Several non-QSO absorption line constraints on $\eta = \eta$ exist, falling into two distinct classes, ‘local’ and ‘early universe’. We direct the reader to the recent review of Uzan (2003) for a summary of these methods.

The local constraints include laboratory comparisons of atomic clocks (Prestage et al. 1995) and fountains (Sortais et al. 2001), analysis of ^{149}Sm isotopic abundances from the Oklo natural fission reactor in Gabon, Africa (Shlyakhter 1976; Damour & Dyson 1996), and meteoritic constraints on the long-lived β -decay rate of ^{187}Re (Peebles & Dicke 1962; Dyson 1967, 1972). The strongest current constraints are, respectively, $j = j = (0.2 \pm 7.5) \times 10^{15}$ ($\eta = 4.7 \text{ yr}$; Marion et al. 2003), $\eta = \eta = (0.04 \pm 0.15) \times 10^7$ ($\eta = 1.8 \text{ G yr}$; Fujii et al. 2000) and $j = j < 3 \times 10^7$ ($\eta = 4.56 \text{ G yr}$; Olive et al. 2002), where η is the relevant look-back time. However, none of these methods constrain η directly: the laboratory measurements assume constant nuclear magnetic moments (Marion et al. 2003), the Oklo bound can be weakened by allowing other interaction strengths and mass ratios to vary (Flambaum & Shuryak 2002; Olive et al. 2002) and Uzan (2003) notes that the meteoritic β -decay limit assumes a constant weak interaction strength, w . Moreover, as discussed in Section 4.3, one can not reliably compare these local limits with MM constraints on $\eta = \eta$ without a detailed theory giving both temporal and spatial variations of η .

The early universe constraints come from analysis of the CMB anisotropies (Hannestad 1999; Kaplinghat, Scherrer & Turner 1999) and light-element (e.g. D, He, Li) big bang nucleosynthesis (BBN) abundances (Kolb, Perry & Walker 1986). The strongest constraints from the CMB are at the $\eta = 10^2$ level if one considers the uncertainties in, and degeneracies with, the usual cosmological parameters (i.e. m , etc.; e.g. Martins et al. 2003). However, Kujat & Scherrer (2000) and Battye, Crittenden & Weller (2001) note a crucial degeneracy between η and m_e . Estimates based on the BBN abundance of ^4He suffer from a large uncertainty as to the electromagnetic contribution to the proton-neutron mass difference. The least model-dependent limits are those of Nollett & Lopez (2002), $\eta = \eta = (3 \pm 7) \times 10^2$, who, like Bergström, Iguri & Rubinstein (1999), considered all light elements up to ^7Li , thereby avoiding this problem. However, Uzan (2003) notes that variations in η are degenerate with variations in w , s and G .

6.4 Future MM method checks

All the alternative methods discussed in the previous two sections constrain η in (sometimes model-dependent) combination with other constants. Therefore, the only current avenue for confidently ruling out the present evidence for varying η is to obtain

independent MM constraints from QSO spectra. The present work has shown that no known systematic errors can mimic the effect of varying α in the Keck/HIRES spectra. However, if subtle, unknown instrumental effects cause the line-shifts we observe, the high quality spectra now available from the VLT/UVES and Subaru/HDS will bear this out. If the present results are confirmed, iodine cell calibration techniques, similar to those used to identify extra-solar planets (e.g. Marcy & Butler 1992), could be applied to selected absorption systems to confidently rule out instrumental effects.

ACKNOWLEDGMENTS

We are indebted to Wallace Sargent for the new Keck/HIRES dataset presented above. Without his extensive and careful observations, as well as the support of numerous co-observers, the present work would not have been possible. We are also grateful to Tom Barlow and Rob Simcoe for their careful data reduction. We greatly appreciate the continued support of, and fruitful discussions with, Chris Churchill, Jason Prochaska and Arthur Wolfe who also provided the previous Keck/HIRES datasets. We also thank Tom Bida and Steve Vogt for detailed information regarding Keck/HIRES, particularly the latter for providing ZEMAX models of the spectrograph. John Barrow, Charley Lineweaver and Jochen Liske contributed valuable ideas and criticisms.

We are grateful to the John Templeton Foundation for supporting this work. MTM received a Grant-in-Aid of Research from the National Academy of Sciences, administered by SigmaXi, the Scientific Research Society. MTM is also grateful to PPARC for support at the IoA under the observational rolling grant (PPA/G/O/2000/00039). JKW thanks the IoA for hospitality while carrying out some of this work. We thank the Australian Partnership for Advanced Computing National Facility for numerically intensive computing access.

Data presented herein were obtained at the W.M. Keck Observatory, which is operated as a scientific partnership among the California Institute of Technology, the University of California and the National Aeronautics and Space Administration. The Observatory was made possible by the generous financial support of the W. M. Keck Foundation.

REFERENCES

- Andrews S. M., Meyer D. M., Lauroesch J. T., 2001, *ApJ*, 552, L73
 Bahcall J. N., Sargent W. L. W., Schmidt M., 1967, *ApJ*, 149, L11
 Bahcall J. N., Steinhart C. L., Schlegel D., 2003, *ApJ*, submitted, preprint (astro-ph/0301507)
 Barrow J. D., O'Toole C., 2001, *MNRAS*, 322, 585
 Battye R. A., Crittenden R., Weller J., 2001, *Phys. Rev. D*, 63, 043505
 Bekenstein J. D., 1979, *Comments on Astrophys.*, 8, 89
 Berengut J. C., Dzuba V. A., Flambaum V. V., 2003, *Phys. Rev. A*, submitted, preprint (physics/0305068)
 Bergström L., Iquri S., Rubinstein H., 1999, *Phys. Rev. D*, 60, 045005
 Bethe H. A., Salpeter E. E., 1977, *Quantum mechanics of one- and two-electron atoms*. Plenum, New York, NY, USA
 Briggs F. H., Wolfe A. M., Turnshek D. A., Schaeffer J., 1985, *ApJ*, 293, 387
 Carilli C. L. et al., 2000, *Phys. Rev. Lett.*, 85, 5511
 Churchill C. W., Le Brun V., 1998, *ApJ*, 499, 677
 Churchill C. W., Mellon R. R., Charlton J. C., Jannuzi B. T., Kirhakos S., Steidel C. C., Schneider D. P., 2000a, *ApJS*, 130, 91
 Churchill C. W., Mellon R. R., Charlton J. C., Jannuzi B. T., Kirhakos S., Steidel C. C., Schneider D. P., 2000b, *ApJ*, 543, 577
 Churchill C. W., Vogt S. S., 2001, *AJ*, 122, 679
 Cowie L. L., Songaila A., 1995, *ApJ*, 453, 596
 Crawford I. A., Howarth I. D., Ryder S. D., Stathakis R. A., 2000, *MNRAS*, 319, L1
 Curran S. J., Murphy M. T., Webb J. K., Rantakyö F., Johansson L. E. B., Nikolić S., 2002, *A&A*, 394, 763
 Damour T., Dyson F., 1996, *Nucl. Phys. B*, 480, 37
 Dent T., Fairbairn M., 2003, *Nucl. Phys. B*, 653, 256
 Dmitriev V. F., Flambaum V. V., 2003, *Phys. Rev. D*, 67, 063513
 Drinkwater M. J., Webb J. K., Barrow J. D., Flambaum V. V., 1998, *MNRAS*, 295, 457
 Drullinger R. E., Wineland D. J., Bergquist J. C., 1980, *Appl. Phys.*, 22, 365
 Dyson F. J., 1967, *Phys. Rev. Lett.*, 19, 1291
 Dyson F. J., 1972, in Salam A., Wigner E. P., eds, *Aspects of Quantum Theory*, Cambridge University Press, Cambridge, UK, p. 213
 Dzuba V. A., Flambaum V. V., Kozlov M. G., Marchenko M., 2002, *Phys. Rev. A*, 66, 022501
 Dzuba V. A., Flambaum V. V., Murphy M. T., Webb J. K., 2001a, in Karshenboim S. G., Pavone F. S., Bassani G. F., Inguscio M., Hänsch T. W., eds, *Lecture Notes in Physics Vol. 570, The Hydrogen Atom: Precision Physics of Simple Atomic Systems*. Springer-Verlag, Berlin, Germany, p. 564
 Dzuba V. A., Flambaum V. V., Murphy M. T., Webb J. K., 2001b, *Phys. Rev. A*, 63, 42509
 Dzuba V. A., Flambaum V. V., Webb J. K., 1999a, *Phys. Rev. A*, 59, 230
 Dzuba V. A., Flambaum V. V., Webb J. K., 1999b, *Phys. Rev. Lett.*, 82, 888
 Edlen B., 1966, *Metrologia*, 2, 71
 Filippenko A. V., 1982, *PASP*, 94, 715
 Fisher R. A., 1958, *Statistical Methods for Research Workers*. Harper, New York, NY, USA
 Flambaum V. V., Shuryak E. V., 2002, *Phys. Rev. D*, 65, 103503
 Fujii Y., Iwamoto A., Fukahori T., Ohnuki T., Nakagawa M., Hidaka H., Oura Y., Möller P., 2000, *Nucl. Phys. B*, 573, 377
 Gay P. L., Lambert D. L., 2000, *ApJ*, 533, 260
 Griesmann U., Kling R., 2000, *ApJ*, 536, L113
 Haehnelt M. G., Steinmetz M., Rauch M., 1998, *ApJ*, 495, 647
 Hallstadius L., 1979, *Z. Phys. A*, 291, 203
 Hannestad S., 1999, *Phys. Rev. D*, 60, 023515
 Herbig G. H., 1975, *ApJ*, 196, 129
 Ivanchik A. V., Rodríguez E., Petitjean P., Varshalovich D. A., 2002, *Astron. Lett.*, 28, 423
 Jenniskens P., Desert F.-X., 1994, *A&AS*, 106, 39
 Kaplinghat M., Scherrer R. J., Turner M. S., 1999, *Phys. Rev. D*, 60, 023516
 Kolb E. W., Perry M. J., Walker T. P., 1986, *Phys. Rev. D*, 33, 869
 Kujat J., Scherrer R. J., 2000, *Phys. Rev. D*, 62, 023510
 Kupka F., Piskunov N., Ryabchikova T. A., Stempels H. C., Weiss W. W., 1999, *A&AS*, 138, 119
 Langacker P., Segrè G., Strassler M. J., 2002, *Phys. Lett. B*, 528, 121
 Lanzetta K. M., Bowen D. V., 1992, *ApJ*, 391, 48
 Lauroesch J. T., Meyer D. M., Blades J. C., 2000, *ApJ*, 543, L43
 Lineweaver C. H., Tenorio L., Smoot G. F., Keegstra P., Banday A. J., Lubin P., 1996, *ApJ*, 470, 38
 Liske J., 2003, *A&A*, 398, 429
 Lu L., Sargent W. L. W., Womble D. S., Takada-Hidai M., 1996, *ApJ*, 472, 509
 Maller A., Somerville R. S., Prochaska J. X., Primack J. R., 1999, in Bunker A. J., van Breugel W. J. M., eds, *ASP Conf. Ser. Vol. 193, The High-Redshift Universe: Galaxy Formation and Evolution at High Redshift*. Astron. Soc. Pac., San Francisco, CA, U.S.A., p. 608
 Marcy G. W., Butler R. P., 1992, *PASP*, 104, 270
 Marion H. et al., 2003, *Phys. Rev. Lett.*, 90, 150801
 Martins C. J. A. P., Melchiorri A., Rocha G., Trotta R., Avelino P. P., Viana P. T. P., 2003, *Phys. Rev. Lett.*, submitted, preprint (astro-ph/0302295)
 Matsubara K., Urabe S., Watanabe M., 2002, in *Proc. Asia-Pacific Workshop on Time and Frequency 2002*. Daejeon, Korea, p. 290
 McDonald P., Miralda-Escudé J., 1999, *ApJ*, 519, 486
 Mohr P. J., Taylor B. N., 2000, *Rev. Mod. Phys.*, 72, 351

Moore C. E., 1971, Atomic Energy Levels as Derived from Analyses of Optical Spectra. Natl. Stand. Rel. Data Ser. Vol. 1–3, Natl. Bur. Stand. (USA), US Govt. Printing Office, Washington DC, USA

Morton D. C., 1991, ApJS, 77, 119

Murphy M. T., Webb J. K., Flambaum V. V., Churchill C. W., Prochaska J. X., 2001b, MNRAS, 327, 1223 (M01b)

Murphy M. T., Webb J. K., Flambaum V. V., Drinkwater M. J., Combes F., Wiklind T., 2001d, MNRAS, 327, 1244

Murphy M. T., Webb J. K., Flambaum V. V., Dzuba V. A., Churchill C. W., Prochaska J. X., Barrow J. D., Wolfe A. M., 2001a, MNRAS, 327, 1208 (M01a)

Murphy M. T., Webb J. K., Flambaum V. V., Prochaska J. X., Wolfe A. M., 2001c, MNRAS, 327, 1237

Nave G., Learner R. C. M., Thorne A. P., Harris C. J., 1991, J. Opt. Soc. Am. B, 8, 2028

Nollett K. M., Lopez R. E., 2002, Phys. Rev. D, 66, 063507

Norlén G., 1973, Phys. Scr., 8, 249

Nulsen P. E. J., Barcons X., Fabian A. C., 1998, MNRAS, 301, 168

Olive K. A., Pospelov M., Qian Y.-Z., Coc A., Cassé M., Vangionis-Flam E., 2002, Phys. Rev. D, 66, 045022

Outram P. J., Carswell R. F., Theuns T., 2000, ApJ, 529, L73

Outram P. J., Chaffee F. H., Carswell R. F., 1999, MNRAS, 310, 289

Palmer B. A., Engleman R., 1983, Technical report, Atlas of the Thorium spectrum. Los Alamos National Laboratory, NM, USA

Peebles P. J., Dicke R. H., 1962, Phys. Rev., 128, 2006

Pickering J. C., Donnelly M. P., Nilsson H., Hibbert A., Johansson S., 2002, A&A, 396, 715

Pickering J. C., Thorne A. P., Murray J. E., Litzén U., Johansson S., Zilio V., Webb J. K., 2000, MNRAS, 319, 163

Pickering J. C., Thorne A. P., Webb J. K., 1998, MNRAS, 300, 131

Piskunov N. E., Kupka F., Ryabchikova T. A., Weiss W. W., Jeffery C. S., 1995, A&AS, 112, 525

Prestage J. D., Tjoelker R. L., Maleki L., 1995, Phys. Rev. Lett., 74, 3511

Price R. J., Crawford I. A., Barlow M. J., 2000, MNRAS, 312, L43

Prochaska J. X., 2003, ApJ, 582, 49

Prochaska J. X., Wolfe A. M., 1999, ApJS, 121, 369

Prochaska J. X., Wolfe A. M., 2000, ApJ, 533, L5

Prochaska J. X. et al., 2001, ApJS, 137, 21

Rao S. M., Turnshek D. A., 2000, ApJS, 130, 1

Rosman K. J. R., Taylor P. D. P., 1998, J. Phys. Chem. Ref. Data, 27, 1275

Savedoff M. P., 1956, Nat, 178, 689

Schaye J., 2001, ApJ, 559, L1

Schneider D. P. et al., 2002, AJ, 123, 567

Shlyakhter A. I., 1976, Nat, 264, 340

Sortais Y. et al., 2001, Phys. Scr., T95, 50

Timmes F. X., Clayton D. D., 1996, ApJ, 472, 723

Timmes F. X., Woosley S. E., Weaver T. A., 1995, ApJS, 98, 617

Uzan J., 2003, Rev. Mod. Phys., 75, 403

Valenti J. A., Butler R. P., Marcy G. W., 1995, PASP, 107, 966

Varshalovich D. A., Panchuk V. E., Ivanchik A. V., 1996, Astron. Lett., 22, 6

Varshalovich D. A., Potekhin A. Y., Ivanchik A. V., 2000, in Dunford R. W., Gemmel D. S., Kanter E. P., Kraessig B., Southworth S. H., Young L., eds, AIP Conf. Proc. Vol. 506, X-Ray and Inner-Shell Processes. Argonne National Laboratory, Argonne, IL, USA, p. 503

Vogt S. S. et al., 1994, in Crawford D. L., Craine E. R., eds, Proc. SPIE Vol. 2198, Instrumentation in Astronomy VIII. p. 362

Walker M., Wardle M., 1998, ApJ, 498, L125

Weast R. C., 1979, Handbook of Chemistry and Physics, 60th edn. CRC Press, Boca Raton, FL, USA

Webb J. K., Flambaum V. V., Churchill C. W., Drinkwater M. J., Barrow J. D., 1999, Phys. Rev. Lett., 82, 884

Webb J. K., Murphy M. T., Flambaum V. V., Dzuba V. A., Barrow J. D., Churchill C. W., Prochaska J. X., Wolfe A. M., 2001, Phys. Rev. Lett., 87, 091301

Whaling W., Anderson W. H. C., Carle M. T., Brault J. W., Zarem H. A., 1995, J. Quant. Spectrosc. Radiat. Transfer, 53, 1

Wolfe A. M., Brown R. L., Roberts M. S., 1976, Phys. Rev. Lett., 37, 179

Wolfe A. M., Prochaska J. X., 2000a, ApJ, 545, 591

Wolfe A. M., Prochaska J. X., 2000b, ApJ, 545, 603

This paper has been typeset from a \LaTeX file prepared by the author.